Regolith-hosted rare earth genesis under humid climates in the Coastal Cordillera of the Central Andes

Nicolás Bustos[1,2], Carlos Marquardt[1,2], Tomás Roquer[1,2], Paulina Vergara[1,2]
[1] Departamento de Ingeniería Estructural y Geotécnica, Pontificia Universidad Católica de Chile, Santiago, Chile
[2] Departamento de Ingeniería de Minería, Pontificia Universidad Católica de Chile, Santiago, Chile

Abstract. Regolith-hosted rare earth element deposits (RH-REE) have been recently found in Chile, nonetheless their ore formation controls, which include temperate to arid climate, intrusive rocks with weatherable REE minerals, and gentle slopes or pediplains, among others, differ from the most common deposits in Asia. This work addresses mineralization and exploration methods for RH-REE deposits across the Chilean Coastal Range. The studied prospect is associated with late Carboniferous I-type tonalitic intrusions. Mineralogical analysis (TIMA-X) indicates that allanite and monazite are the main REE-bearing minerals in the host rock. The regolith in the study area is up to 60 m deep and contains an exchangeable-REE concentration up to 2000 ppm, as determined by portable X-ray fluorescence (pXRF) and ICP-MS. We were able to recognize that REE-adsorption takes place both in preserved and partially eroded regoliths. Progressive weathering of these regoliths causes the pedolith/saprolith limit to be dynamic and accumulate REE due to the breakdown of allanite and monazite. Our data shows that the search for pediplains on suitable lithologies, mapping of regolith profiles, and their analysis via pXRF by quantifying yttrium, appears to be a suitable strategy for early exploration of RH-REE deposits in the Chilean Coastal Range.

1 Introduction

The rare earth elements (REE) correspond to the 15 elements of the lanthanides, plus Sc and Y (due to geochemical similarities). These elements have high geochemical affinity among each other and are divided, according to their atomic number and their different physiochemical and geochemical properties, into light (LREE: La–Eu) and heavy rare earth elements (HREE: Gd–Lu) (Sanematsu and Watanabe 2016).

In RH-REE deposits, REE are transported by meteoric fluids during weathering and adsorbed by neoformed clay minerals (Foley and Ayuso 2015), such as kaolinite, halloysite, and illite, under appropriate climatic and topographic conditions. Later preservation of these REE-rich regolith horizons from erosion depends on underground water flow and erosion controls. These ore formation constraints can be met in various areas of the planet that are underexplored for RH-REE.

RH-REE deposits occur within the Chilean Coastal Range (https://www.aclara-re.com/) since they meet suitable geological and climatic criteria (Sanematsu and Watanabe 2016; Li et al. 2017). These include granitic I-type lithologies with weatherable REE-minerals, deep regoliths (locally up to 60 m), low-slope paleosurfaces, and a temperate climate that would allow the occurrence of supergene pedogenetic processes during which the enrichment of exchangeable REE could take place. The key element that varies between well-known Asian deposits and the ones found in the Coastal Cordillera is the climate setting; this directly affects pediment preservation and formation.
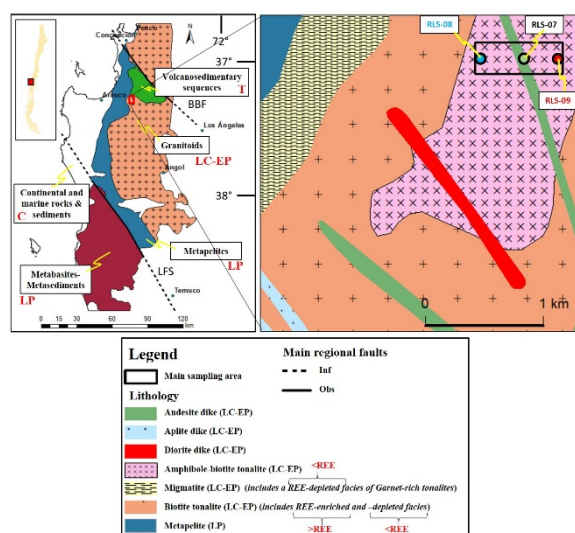
Figure 1. Regional and local geological maps. BBF: Biobío Fault System. LFS: Lanalhue Fault System. C: Cenozoic. T: Triassic. LC-EP: late Carboniferous to early Permian. LP: late Paleozoic. Regional case adapted and simplified from Alarcón and Álvarez (2019) and Glodny et al. (2008).

2 Methodology

2.1 Sampling information

A specific work area was determined to search and map outcrops of fresh rocks and regoliths which are favorable to the formation of RH-REE, namely amphibole-biotite tonalite and biotite tonalite (see Figure 1). In the work area, a more focused sampling area was selected after searching for a geomorphically suitable spot in terms of deep regolith formation and low slope pediplains or potential pediments.

2.2 Geochemical, petrographic, and geomorphic characterizations

The samples analyzed with ICP-MS include regolith samples obtained from 32 drillholes (total of 319 sub-samples when considering meter-by-meter compositing), as well as one rock sample obtained on the surface. The drillhole samples were analyzed

to quantify the exchangeable-REE fraction (ICP-MS_DD) and the surface samples were analyzed for total rock (ICP-MS_T).

The samples analyzed for geochemistry were checked with QA/QC by the mining firm. The samples' desorption was carried out in two stages (hence, DD: "double desorption") to replicate the recovery obtained by the industrial-scaled metallurgical process, whilst stabilizing the pH at 4 throughout the process by adding drops of H_2SO_4 (sulfuric acid) and NH_4OH (ammonium hydroxide). These two sequential desorptions utilized $(NH_4)_2SO_4$ (ammonium sulfate) at 0.4 M and distilled water as leaching agents to release the exchangeable ions into the solution for later ICP-MS analysis.

The pXRF analysis of the samples was carried out with a Niton® XL3t GOLDD+ instrument, which was used to perform a total rock analysis focusing on trace elements (pXRF_T). The analysis and sample manipulation were based on established methods, and the samples fulfilled standards that maximize the precision of the analyses: moisture content, granulometry, container, thickness of sample, and analysis time.

Petrographic analyses were conducted with the automatic mineralogy instrument TIMA-X (TESCAN Integrated Mineral Analyzer), to characterize the mineralogy of each lithology. The instrument is equipped with four EDS EDAX Element 30 detectors and the analyses were carried out with an 8.0 µm resolution and 1000 counts per pixel. This technology cannot correctly identify minerals with concentrations <0.1%.

In terms of remote geomorphology, we propose an adaptation of Bowles and Cowgill's (2012) methodology to identify marine terraces. Using this methodology, it was sought to generate, starting from slope and roughness maps, a map known as a Surface Classification Model (SCM). Besides the experience provided by the cited article, information from swath profiles and satellite maps was used to identify geomorphic targets with high pediment quality (see Figure 2).
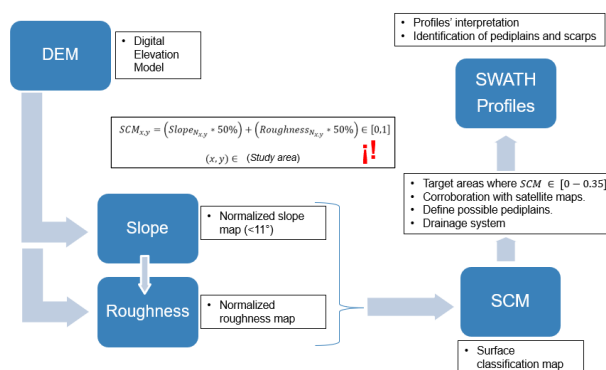
Figure 2. Morphometric methodology and sequential steps towards identification of targets where RH-REE deposits could be preserved.

3 Geological framework

Within the study area, a Paleozoic metamorphic unit of metapelite presents a contact aureole characterized by migmatite outcroppings due to late Carboniferous–early Permian granitic intrusions (Alarcón and Álvarez 2019). The granitic units are composed mainly of biotite tonalite and amphibole-biotite tonalite (Figure 1). They have been described under mineralogical and geochemical criteria as I-type (Hervé et al. 1988; Creixell 2001), and are, thus, a potential source for RH-REE mineralization.

These tonalitic intrusions have a higher potential to form RH-REE deposits because: (1) geochemical, mineralogical, and petrographic analyses of fresh rock samples have proven the existence of elevated REE concentrations; and (2) they correspond to the preferential lithology (granitoids) reported by several authors in terms of regolith formation and REE-adsorption processes (e.g., Sanematsu and Watanabe 2016; Li et al. 2017; Li et al. 2019).

The local tonalites formed from calc-alkaline magmas generated in an active continental margin (Creixell 2001). The tonalites crystalized at a lower temperature (~600 °C), compared to other granitic non-marginal facies of the larger pluton (up to 700 °C), due to an additional H2O contribution from the dehydration of the host rock (Creixell 2001). The tonalites have metaluminous composition (A/CNK = 0.77–0.98), whereas existent garnet-rich marginal facies have peraluminous composition (A/CNK = 1.01). Granite discrimination diagrams classify the tonalites as low-K and sub-alkaline (Creixell 2001).

4 Geomorphic framework

The study area has currently a temperate climate with a mean annual temperature of 12.9 °C and mean annual precipitation of 715.6 mm (Dirección Meteorológica de Chile 2020). These conditions are thought to have been rather stable during the Quaternary. The field observations showed that regoliths that were developed upon local intrusive rocks could reach thicknesses of up to 60 m.

Two families of soil profiles are described within the study area. On one hand, there is the case of highly preserved regoliths (Figure 3A), where exchangeable-REE mineralization occurs exactly along the contact between the pedolith and saprolith. On the other hand, some regoliths show evidence of higher local erosion rates (Figure 3B), as the original pedolith was partly removed; here, the upper layers correspond to a thinner newly formed pedolith with an important re-concentration of exchangeable REE. Evidence of these higher local erosion rates is, chiefly, the lack of depletion zones of mobile elements at the top of the regolith profile.
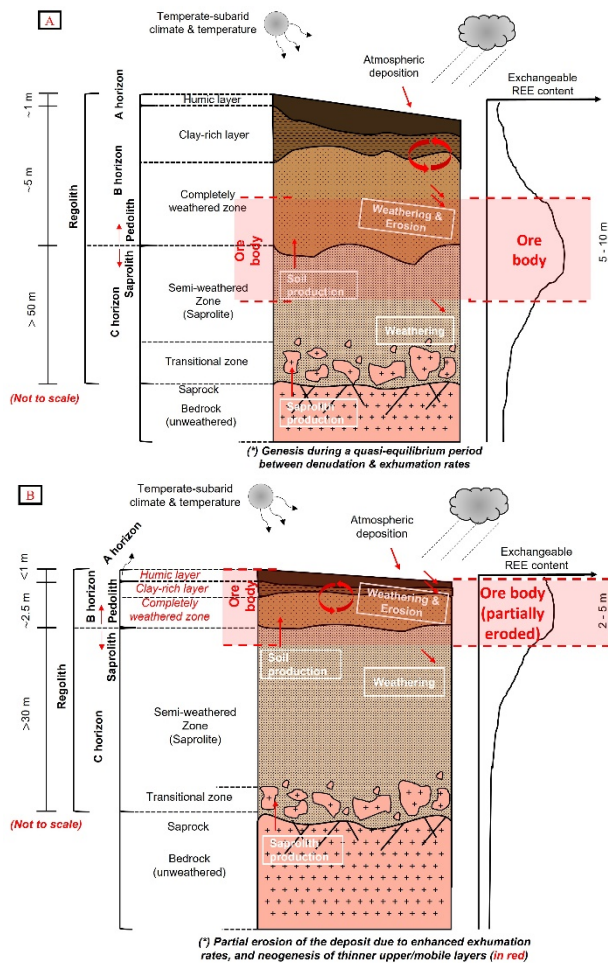
Figure 3. a Preserved regolith profiles. b Partially eroded regolith profiles.

5 Geochemical results from drillholes

Based on the TIMA-X analyses, two main REE-bearing minerals (both LREE-dominant) were identified: allanite, $Ca_2(Ce,La)(Al_2Fe^{2+})[Si_2O_7]$ $[SiO_4]O(OH)$, and monazite, $(Ce,Nd,La)(PO_4)$. Two other REE-bearing minerals were also detected, although at much lower concentrations: parisite (LREE-dominant) and xenotime (HREE+Y-dominant).

The obtained data (Figures 4,5) show the variation of major elements across the soil profile and their relationship to yttrium concentration, which encompass the accumulation zone of exchangeable REE, and with mobile elements (Ca, K, Sr). Furthermore, the REE-dominance and concentration of the ore body of each drillhole is showed.

The evolution of several geochemical ratios across preserved and partially eroded regoliths is presented in Figure 5. It is shown that LREE predominate in shallow horizons of the regolith; this can be proven be checking the evolution of $(La/Yb)_N$ and how this ratio progressively decreases towards deeper zones (6–2).

In partially eroded regoliths, this behaviour is very similar, although it begins with lower values, due to local erosion. Finally, among preserved regoliths, the

cerium anomaly (Ce/Ce*) has a rising trend with increasing depth but remains as a negative anomaly (i.e., Ce/Ce* < 1) down to a depth of 10 m.
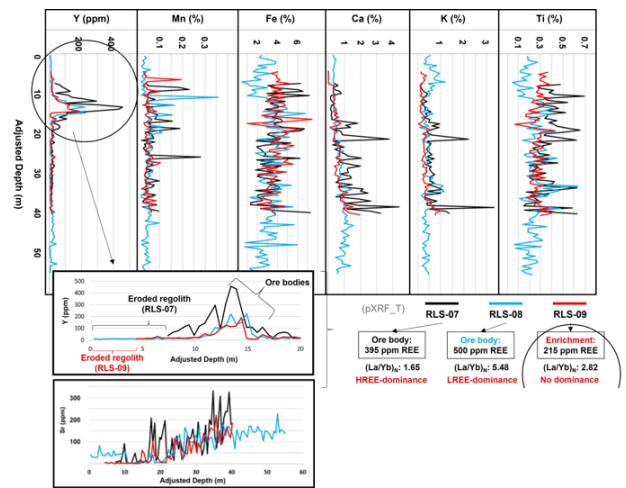

Figure 4. Concentrations of major elements and yttrium across the regolith profiles of three drillholes obtained by portable X-ray fluorescence (pXRF) analysis. pXRF_T: pXRF (total fraction).
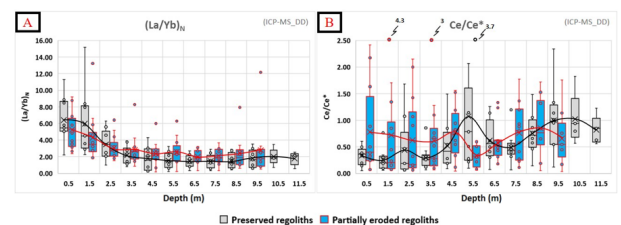

Figure 5. Variation of geochemical ratios across the regolith profile. ICP-MS_DD: ICP-MS (exchangeable fraction). a Normalized Lanthanum-Ytterbium ratio. b Cerium anomaly.

6 Analytic conciliation: approximation for an RH-REE-deposit model

The morphometric analysis of the study area is indeed placed upon a preferential zone with SCM values <0.35. This can be seen more detailed in Figure 6.
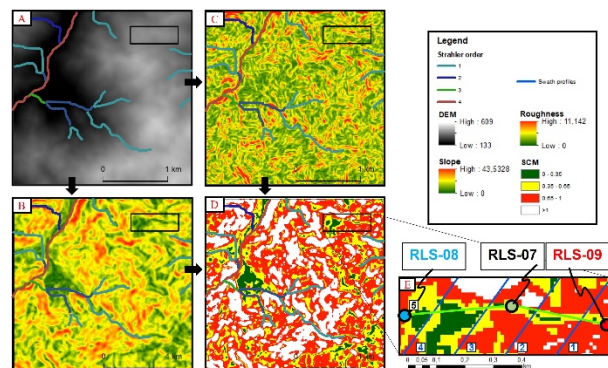
Figure 6. Results of the morphometric analysis. a DEM (12.5-m resolution). b Slope map. c Roughness map. d Normalized SCM map. e SCM map magnification. The maps also include the drainage system (Strahler method).
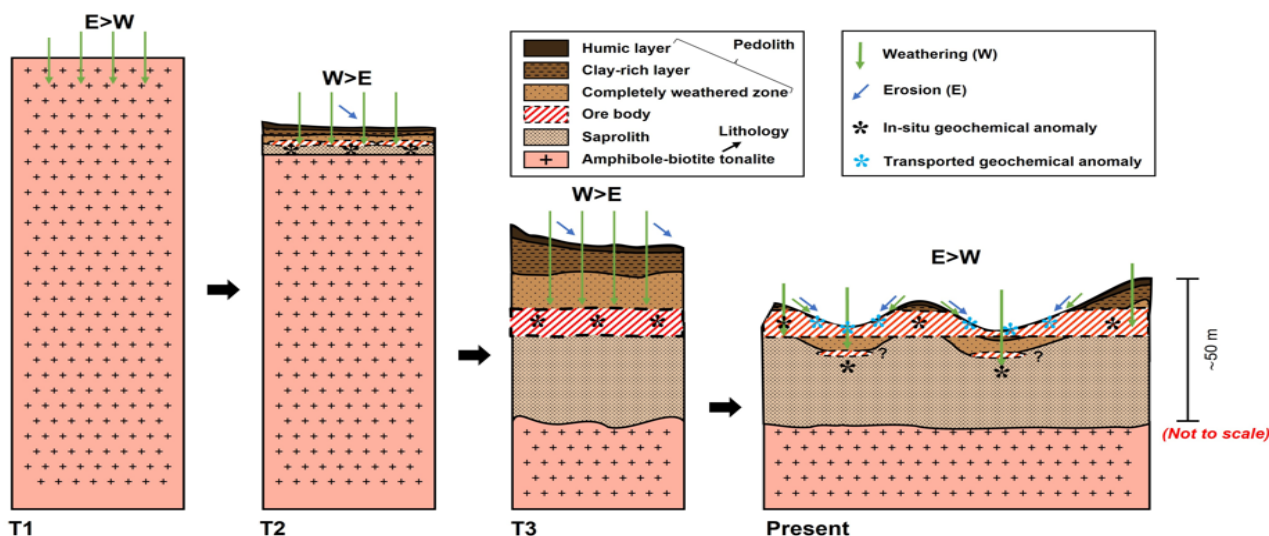
Figure 7. Scheme of the geomorphic evolution proposed for RH-REE deposits in the region. T1: Pediment formation. T2: Start of chemical and physical weathering processes; REE transportation takes place, and the enriched fluids permit a first adsorption and previous secondary clay mineral formation. T3: genesis of the RH-REE deposit due to adsorption; at this point, the erosion rates increase. Present: erosion of the local morphology due to the development of drainage systems; deposit's partial/local erosion.

The differences between preserved and partially eroded regoliths demand a process able to account for both chemical and physical differences in these profiles. We suggest that preserved regoliths - and the REE mineralization associated with them - represent an early pedogenetic process that was fully preserved from erosion. Partially eroded regoliths, on the other hand, underwent a second pedogenetic stage that was able to re-fractionate the REE, or even that some elements are preferentially adsorbed under specific environments, such as pH, temperature, or exchange capacity of secondary clays. Thus, the large increase of REE ratios within exposed mineralized horizons of partially eroded regoliths could be explained by shallow and younger enrichment processes. These processes were likely lateral leaching events that affect REE-rich minerals that are more susceptible to chemical weathering under shallow conditions.

7 Conclusions

We were able to detect, describe, and discuss the essential geological processes that led to the formation of RH-REE deposits where both hypogene and supergene processes are involved. The final ore control processes require regolith formation and evolution: (1) exhumation and pediment formation, (2) development of deep weathering profiles (i.e., REE-remobilization: REE-precipitation into secondary minerals and REE-adsorption onto clay minerals), and (3) preservation of the mineralized bodies. For the time being, the reconciliation of geomorphic and petrographic information, that is,

the search for pediplains and favorable regoliths developed on adequate lithologies, appears to be a suitable method for addressing the problem of exploring for RH-REE deposits in Coastal Cordillera.

Acknowledgements

References

Alarcón, A., Álvarez, F., 2019. Caracterización óptica y composicional del concentrado de minerales de uranio, torio y tierras raras en las pegmatitas de poñen y Parque Coyanmahuida. Universidad de Concepción, Concepción, Chile (undergraduate thesis).

Bowles, C., Cowgill, E., 2012. Discovering marine terraces using airborne LiDAR along the Mendocino-Sonoma coast, northern California. Geosphere 8 (2), 386–402.

Creixell, C., 2001. Petrología y Geotermobarometría de las Rocas Intrusivas de la Cordillera de la Costa entre los 36°30' y 38°00' S. Universidad de Concepción, Concepción, Chile (undergraduate thesis).

Foley, N., Ayuso, R., 2015. REE enrichment in granite-derived regolith deposits of the Southeastern United. In: Geological Survey, 131-138. States: Prospective Source Rocks and Accumulation Processes.

Glodny, J., Echtler, H., Collao, S., Ardiles, M., Burón, P., Figueroa, O., 2008. Differential late Paleozoic active margin evolution in South-Central Chile (37°S–40°S) – the Lanalhue Fault Zone. J. S. Am. Earth Sci. 26, 397–411.

Hervé, F., Munizaga, F., Parada, M., Brook, M., Pankhurst, R., Snelling, N., Drake, R., 1988. Granitoids of the Coast Range of Central Chile: geochronology and geologic setting. J. S. Am. Earth Sci. 1 (2), 185–194.

Li, M., Zhou, M., Zhao, W., 2017. Nature of parent rocks, mineralization styles and ore genesis of regolith-hosted REE deposits in South China: an integrated genetic model. J. Asian Earth Sci. 148, 65–95.

Li, M., Zhou, M., Williams-Jones, A., 2019. The genesis of regolith-hosted heavy rare earth element deposits: insights from the world-class Zudong Deposit in Jiangxi Province, South China. Econ. Geol. 114, 541–568.

Sanematsu, K., Watanabe, Y., 2016. Characteristics and genesis of ion adsorption-type rare Earth element deposits. Rev. Econ. Geol. 18, 55–79.

Mn-Ni-Co oxy-hydroxides from Ni-Co laterites of Moa-Bay mining district, eastern Cuba

Diego Domínguez-Carretero[1], Cristina Villanova-de-Benavent[1], Cristina Domènech[1], Joaquín A. Proenza[1]
[1]*Departament de Mineralogia, Petrologia i Geologia Aplicada, Facultat de Ciències de la Terra, Universitat de Barcelona (UB), Spain*

Abstract. Ni and Co have been listed as critical energy metals for a sustainable economic development by several government agencies. Ni-Co laterite deposits are among the first resources of both metals in the world. The correct identification of Ni- and Co-bearing mineral phases is essential to increase the efficiency of extraction of both metals in these deposits. Mn-Ni-Co oxy-hydroxides are key mineral phases because they contain important Ni and Co concentrations. In this study, we have investigated the chemical differences among Mn-Ni-Co oxy-hydroxides formed in the saprolitic and limonitic horizons from lateritic deposits of the Moa Bay lateritic mining district (eastern Cuba). Mn-Ni-Co oxyhydroxides formed in the saprolitic horizons are classified as Ni-asbolane and lack Al and Co. They would have formed at slightly alkaline conditions (pH < 8). Conversely, the ones formed in the limonitic horizon are more enriched in Ni, Co and Al, and poor in Mg, being catalogued as lithiophorite and lithiophorite-asbolane intermediates, and would have formed at more acidic (pH ~ 6) and oxidizing conditions. Finally, several hundreds of ppm of Sc have been measured in Mn-Ni-Co oxyhydroxides from the limonitic horizon, therefore making these minerals interesting targets for the potential extraction of this critical metal as a by-product.

1 Introduction

Ni-Co laterite deposits, formed by the chemical and mechanical weathering of ultramafic rocks, account for 60% of Ni and 37% of Co worldwide resources (Newsome et al., 2019; USGS, 2021). Both metals have been classified by several government agencies (e.g., Australia's National Science Agency, Department of Natural Resources Canada, United States Geological Survey) as critical due to their numerous applications in the steel and electric battery industries. Nowadays, Cuban laterites contain up to 6% of Ni and 7% of Co worldwide reserves (USGS, 2021).

The ore mineralogy in Ni-Co laterites is complex and very heterogeneous. There are still knowledge gaps regarding which mineral phases contain Ni and/or Co, thus making the metallurgical processes inefficient (Elias, 2002; Hernández et al., 2007; Marsh et al., 2013).

In this study, we focus on a detailed characterization of Mn-Ni-Co oxy-hydroxides, a chemically heterogeneous group of ore minerals with highly variable Ni and Co contents. Hence, we have analyzed different samples from the saprolitic and the limonitic horizons of the world-class oxide-type lateritic mining district of Moa Bay (eastern Cuba). These new data allow the chemical distinction between Mn-Co-Ni oxy-hydroxides formed in the saprolitic and limonitic horizons, and ultimately to better understand their formation processes.

2 Geological Setting

Eastern Cuba contains the largest exposure of ophiolitic rocks across the Cuban ophiolitic belt, grouped into the so-called Mayarí-Baracoa Ophiolite Belt (MBOB). The MBOB is Cretaceous in age (90-136 Ma; Iturralde-Vinent et al. 2016; Rojas-Agramonte et al. 2016; Proenza et al. 2018) and it is divided into the Mayarí-Cristal (western part) and the Moa-Baracoa (eastern part) massifs. The Mayarí-Cristal massif is mainly formed by a 5 km thick, highly serpentinized harzburgite tectonite, crosscut by several generations of websterite and gabbro dykes of Island Arc Tholeiite (IAT) affinity (Marchesi et al. 2006, 2007). The ultramafic rocks overthrust a crustal unit consisting of gabbros, microgabbros and abundant diabase dikes (Proenza et al. 1999; Marchesi et al. 2006, 2007). The Moa-Baracoa massif, on the other hand, is composed by a 2.2 km thick mantle-tectonite harzburgite with subordinate dunite and a very well-preserved Moho Transition Zone (MTZ). Layered and isotropic gabbros and pillow basalts with a back-arc geochemical affinity are tectonically overlain by the mantle sequence (Proenza et al. 2006, 2018; Marchesi et al. 2006, 2007).

Eastern Cuba contains one of the largest Ni-Co laterite mining provinces in the world, of about 100 km^2 (Lewis et al., 2006), which includes important mining districts such as Moa Bay (hosted within the Moa-Baracoa massif; Fig.1), Pinares de Mayarí or Nicaro. The laterization of the Moa Bay serpentinites started in the Miocene and continued until the present-day (Lewis et al., 2006 and references therein).

The Mn-Ni-Co oxy-hydroxides studied in this work were obtained from the oxide-type deposits of Yagrumaje Norte and Punta Gorda, with thick limonitic horizons, and from the hydrous Mg-silicate type deposit of Yamanigüey, with a large saprolitic horizon, all belonging to the Moa Bay district.

3. Analytical methods

Polished thin-sections from laterite samples of the studied deposits were analyzed, in a first stage, under a conventional petrographic polarized light microscope at the Universitat de Barcelona (UB) and later, by scanning electron microscopy using a JEOL JSM-7100 field-emission SEM at 20 kV and 5 nA at

the Centres Científics i Tecnològics of the same university (CCiT-UB).

Quantitative electron microprobe analyses (EMPA) on Mn-Ni-Co oxy-hydroxides were also conducted at the CCiT-UB, in a JEOL JXA-8230 equipped with five wavelength-dispersive spectrometers (WDS) operating at 15 kV and 15 nA, with a 1-2 μm beam diameter and 10-30 s (3 minutes in the case of Sc) counting time per element. Wollastonite (Si), corundum (Al), orthoclase (K), hematite (Fe), periclase (Mg), rhodonite (Mn), NiO (Ni), metallic Co (Co), rutile (Ti), Cr2O3 (Cr), metallic Sc (Sc) were used as standards.
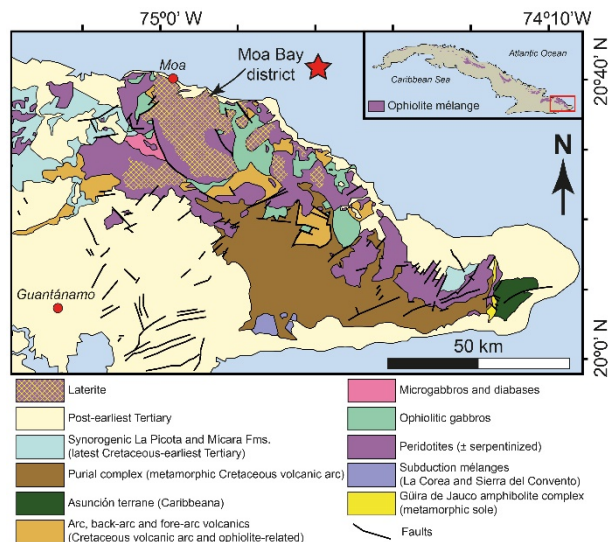
Figure 1. Geological map of the Moa-Baracoa massif (Eastern Cuba) with the location of the Moa Bay Ni-Co laterite mining district.

4. Mineral petrography and chemistry

The studied Mn-Ni-Co oxy-hydroxides from the limonitic and saprolitic horizons differ regarding their textures and chemical composition.
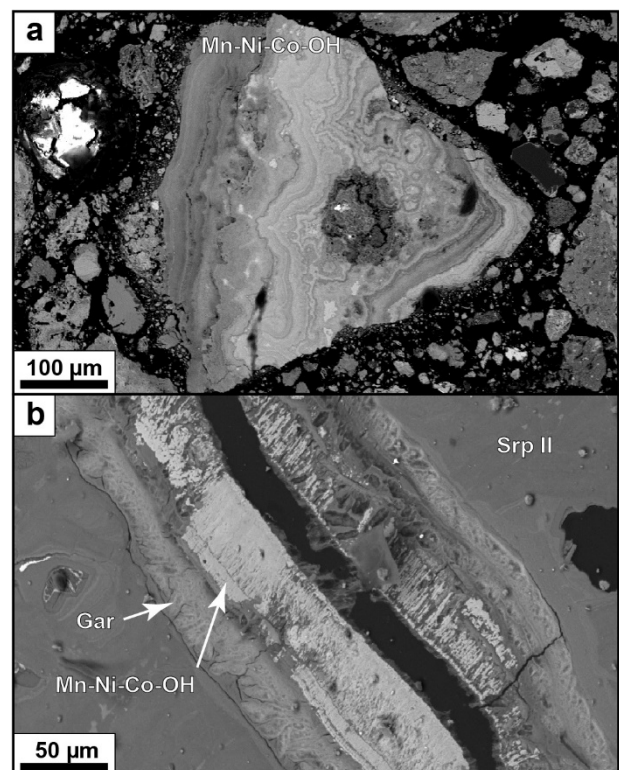
4.1 Limonitic horizon

Samples from the limonitic horizons of Punta Gorda and Yagrumaje Norte deposits consist mainly of goethite with minor amounts of gibbsite, hematite, maghemite, Cr-spinel and Mn-Ni-Co oxy-hydroxides. Mn-Ni-Co oxy-hydroxides are found either replacing goethite or as colloform aggregate individual grains (Fig. 2a) with significant variations in Mn, Co, Ni (Fig. 3), Fe and Al contents. The chemical composition of Mn-Ni-Co oxy-hydroxides shows high variations in MnO (21.5-69.7 wt.%; median value of 36.9 wt.%), FeO (0.45-27.7 wt.%; median value of 3.60 wt.%), NiO (0.8-19.8 wt.%; median value of 10.6 wt.%), Al$_2$O$_3$ (1.25-19.7 wt.%; median value of 6.10 wt.%) and CoO (0.75-10.2 wt.%; median value of 6.41 wt.%). The analyzed grains have low concentrations of K$_2$O (median values of 1.79 wt.%), MgO (median value of 0.49 wt.%) and SiO$_2$ (median value of 0.42 wt.%). The

analyzed Mn-Ni-Co oxy-hydroxides from Punta Gorda yield up to 204 ppm Sc.
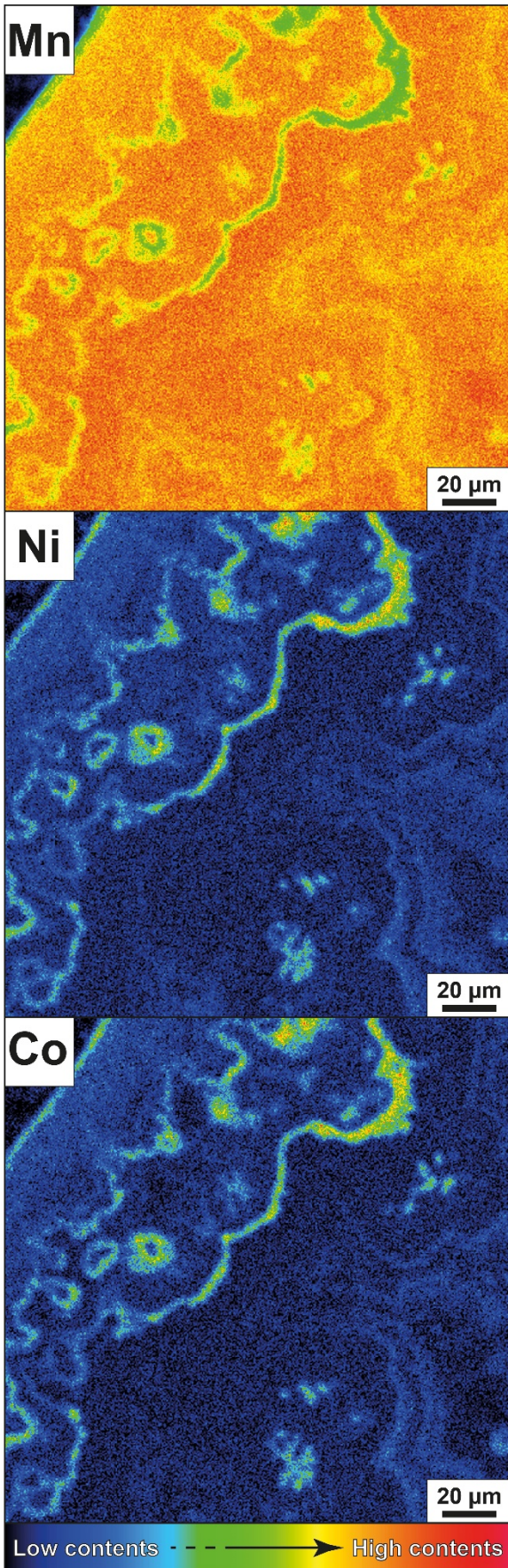
4.2 Saprolitic horizon

The studied samples from the saprolitic horizon of Yamanigüey deposit are mainly composed by serpentine, Ni-rich secondary serpentine, with minor magnetite, Cr-spinel, garnierite and Mn-Ni-Co oxy-hydroxides. The studied Mn-Ni-Co oxy-hydroxides are found as fibrous crystals replacing garnierite in veins crosscutting secondary serpentine (Fig. 2b). Regarding their chemical composition, the analyzed grains have high concentrations of MnO (34.6-56.6 wt.%; median value of 52.2 wt.%), moderate concentrations of MgO (6.5-13.2 wt.%; median value of 7.58 wt.%), NiO (4.68-7.46 wt.%; median value of 5.95 wt.%), SiO$_2$ (2.49-21.2 wt.%; median value of 5.04 wt.%), FeO (1.35-4.71 wt.%; median value of 1.68 wt.%), and very low concentrations of CoO (up to 0.27 wt.%) and Al$_2$O$_3$ (up to 0.02 wt.%).

Figure 2. a) Mn-Ni-Co oxy-hydroxides from the limonitic horizon of the Punta Gorda deposit with colloform texture. b) Fibrous Mn-Ni-Co oxy-hydroxides from the saprolitic horizon of the Yamanigüey deposit in a garnierite vein crosscutting Ni-rich secondary serpentine. Abbreviations: Mn-Ni-Co-OH: Mn-Ni-Co oxy-hydroxide; Gar: Garnierite; Srp II: Ni-rich secondary serpentine.

5. Final remarks

The studied Mn-Ni-Co oxy-hydroxides have a distinctive composition in the limonitic and in the saprolitic horizon. Mn-Ni-Co oxy-hydroxides from the

Figure 3. EMPA elemental maps for Mn, Ni and Co from a colloform Mn-Ni-Co oxy-hydroxide from the limonitic horizon of the Punta Gorda deposit.

saprolitic horizon have high Mg and Mn contents, and have almost no Al nor Co, and are clearly classified as Ni-asbolanes (Fig. 4). However, Mn-Ni-Co oxy-hydroxides from the limonitic horizon have very low Si and Mg contents and higher Al and Co, and they are classified as lithiophorite-asbolane intermediates or as lithophorite (Fig. 4). Consequently, as Co in laterite deposits is still exploited as a by-product, in terms of metal extraction, lithiophorite and lithiophorite-asbolane intermediates from the limonitic horizon (enriched in Ni and Co) represent a more attractive target than the Ni-asbolane from the saprolitic horizon (enriched exclusively in Ni).

Ni-asbolane in the saprolitic horizon is replacing garnierite, whose formation is associated with aqueous, alkaline (pH > 8), Ni-rich solutions (Villanova-de-Benavent et al., 2014). Consequently, Ni-asbolane formation might take place at slightly more acidic conditions, in which garnierite solubility increases.

Lithiophorite and lithiophorite-asbolane intermediates, very abundant in the limonitic horizon (Fig. 4), present either as a newly formed mineral aggregate or replacing previous Fe-oxy-hydroxides, would form under acidic (pH ~ 6) and oxidizing (Eh > 0V) conditions (Llorca, 1993).

Scandium is another critical metal that can be extracted from Ni-Co laterites as a by-product (Wang et al., 2011). Scandium content in laterites is highly correlated with their Fe_2O_3 content (Audet, 2008; Aiglsperger et al., 2016), as Sc may substitute Fe^{3+} in the goethite crystal structure (Levard et al., 2018). However, our preliminary results show how Mn-Ni-Co oxy-hydroxides, specifically lithiophorite and lithiophorite-asbolane intermediates enriched in Al, can contain several hundreds of ppm of Sc, making Mn-Ni-Co oxy-hydroxides a target mineral not only for Ni and Co, but also for Sc.
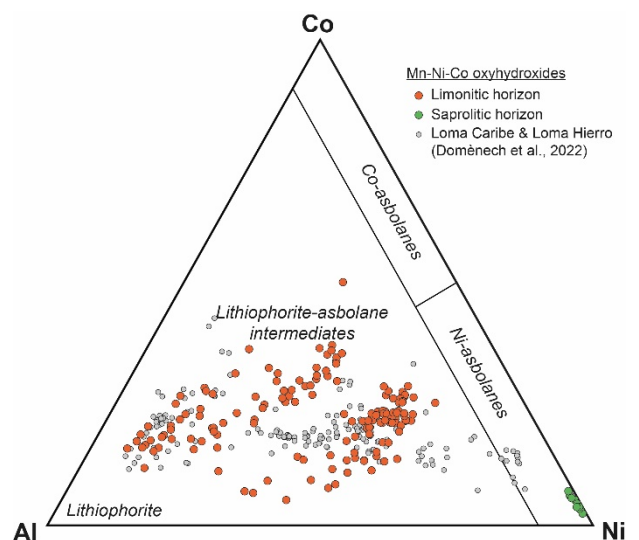
Figure 4. Ternary plot representing Mn, Ni and Co in cation proportions on the basis of 100 oxygens obtained from EMPA analyses on Mn-Ni-Co oxy-hydroxides.

In conclusion, our results show how the precipitation of Mn-Ni-Co oxy-hydroxides is controlled by the Eh-pH variations along the lateritic profile as proposed by Llorca (1993). During early stages of weathering, in the saprolitic zone, at slightly alkaline conditions, Ni-rich asbolane precipitates and replaces silicates, such as serpentine or garnierite. However, during more advanced stages of weathering, in the limonitic zone, when the conditions are oxidizing and slightly acidic, Ni-rich asbolane is not stable any longer, and asbolane-lithiphorite intermediates and lithiphorite precipitate.

Acknowledgements

References

Aiglsperger, T., Proenza, J.A., Lewis, J.F., Labrador, M., Svotjka, M., Rojas-Purón, A., Longo, F., Durisova, J. (2016). Critical metals (REE, Sc, PGE) in Ni laterites from Cuba and the Dominican Republic. Ore Geology Reviews 2016 73, 127-147.

Audet, M.A. (2008). Le massif du Koniambo, Nouvelle-Calédonie Formation et obduction d'un complexe ophiolitique du type SSZ. Enrichissement en nickel, cobalt et scandium dans les profils résiduels (PhD thesis (in French), 327 pp.).

Domènech, C., Villanova-de-Benavent, C., Proenza, J.A., Tauler, E., Lara, L., Galí, S., Soler, J.M., Campeny, M., Ibañez-Insa, J. (2022). Co–Mn Mineralisations in the Ni Laterite Deposits of Loma Caribe (Dominican Republic) and Loma de Hierro (Venezuela). Minerals 12, 927.

Elias, M. (2002). Nickel laterite deposits – geological overview, resources and exploitation. Centre for Ore Deposit Research, University of Tasmania, Special Publication, 4, 205-220.

Hernández, C. M., Banza, A., Gock, E. (2007). Recovery of metals from Cuban nickel tailings by leaching with organic acids followed by precipitation and magnetic separation. Journal of Hazardous Materials, 139, 25–30.

Iturralde-Vinent, M.A., Garcia-Casco, A., Rojas-Agramonte, Y., Proenza, J.A., Murphy, J.B., Stern, R.J. (2016). The geology of Cuba: A brief overview and synthesis. GSA Today 26, 4-10.

Levard, C., Borschneck, D., Grauby, O., Rose, J., Ambrosi, J.P. (2018). Goethite, a tailor-made host for the critical metal scandium:The $Fe_xSc_{(1-x)}OOH$ solid solution. Geochemical Perspectives Letters 9, 16-20.

Lewis, J.F., Draper, G., Proenza, J.A., Espaillat, J., Jimenez. J. (2006). Ophiolite- Related Ultramafic Rocks (Serpentinites) in the Caribbean Region: A Review of their occurrence, Composition, Origin, Emplacement and Nickel Laterite Soils. Geologica Acta 4, 237-263.

Llorca, S.M. (1993). Metallogeny of supergene cobalt mineralization, New Caledonia. Australian Journal of Earth Sciences, 40, 377-385.

Marchesi, C., Garrido, C.J., Godard, M., Proenza, J.A., Gervilla, F., Blanco-Moreno, J. (2006). Petrogenesis of highly depleted peridotites and gabbroic rocks from the Mayarí-Baracoa Ophiolitic Belt (eastern Cuba). Contributions to Mineralogy and Petrology 151(6),717.

Marchesi, C., Garrido, C.J., Bosch, D., Proenza, J.A., Gervilla, F., Monié, P., Rodriguez-Vega, A. (2007). Geochemistry of Cretaceous magmatism in eastern Cuba: recycling of North American continental sediments and implications for subduction polarity in the Greater Antilles Paleo-arc. Journal of Petrology 48, 1813–1840.

Marsh, E., Anderson, E., Gray, F. (2013). Nickel-cobalt laterites—A deposit model, chapter H of Mineral deposit models for resource assessment: U.S. Geological Survey Scientific Investigations Report 2010–5070–H, 38 p.

Newsome, L., Arguedas, A.F.S., Coker, V., Boothman, C., Lloyd, J. (2019). Manganese and cobalt redox cycling in laterites; Biogeochemical and bioprocessing implications. Chemical Geology, 531, 119330.

Proenza, J.A., Díaz-Martínez, R., Iriondo, A., Marchesi, C., Melgarejo, J.C., Gervilla, F., Garrido, C.J., Rodríguez-Vega, A., Lozano-Santacruz, R., Blanco-Moreno, J.A. (2006). Primitive island-arc Cretaceous volcanic rocks in eastern Cuba: the Téneme Formation. Geologica Acta 4, 103-121.

Proenza, J.A., Gervilla, F., Melgarejo, J.C., Bodinier, J.L. (1999). Al- and Cr-rich chromitites from the Mayarí-Baracoa ophiolitic belt (eastern Cuba); consequence of interaction between volatilerich melts and peridotites in suprasubduction mantle. Economic Geology 94, 547-566.

Proenza, J.A., González-Jiménez, J.M., Garcia-Casco, A., Belousova, E., Griffin, W.L., Talavera, C., Rojas-Agramonte, Y., Aiglsperger, T., Navarro-Ciurana, D., Pujol-Solà, N., Gervilla, F., O'Reilly, S.Y., Jacob, D.E. (2018). Cold plumes trigger contamination of oceanic mantle wedges with continental crust-derived sediments: Evidence from chromitite zircon grains of eastern Cuban ophiolites. Geoscience Frontiers 9(6), 1921–1936.

Rojas-Agramonte, Y., Garcia-Casco, A., Kemp, A., Kröner, A., Proenza, J.A., Lázaro, C., Liu, D. (2016). Recycling and transport of continental material through the mantle wedge above subduction zones: A Caribbean example. Earth and Planetary Science Letters 436, 93–107.

Villanova-de-Benavent, C., Proenza, J.A., Galí, S., García-Casco, A., Tauler, E., Lewis, J.F., Longo, F. (2014). Garnierites and garnierite: textures, mineralogy and geochemistry of garnierites in the Falcondo Ni-laterite deposit, Dominican Republic. Ore Geology Reviews 58, 91–109.

Wang, W., Pranolo, Y., Cheng, C.Y. (2011). Metallurgical processes for scandium recovery from various resources: a review. Hydrometallurgy 108, 100–108

USGS (2021). Mineral Commodity Summaries 2021: US Geological Survey; US Geological Survey: Reston, VA, USA; 200p.

Clay-hosted REE mineralisation under the microscope

Michael Gazley[1,2], Manuel Knorsch[3], Kat Lilly[1], Muhammet Kartal[3], Eliza Trunfull[3], Agnieszka Piechocka[3]
[1]*RSC, 225 Thorndon Quay, Wellington, New Zealand*
[2]*School of Geography, Environment and Earth Science, Victoria University of Wellington, New Zealand*
[3]*RSC, 15 Rheola St, West Perth, Australia*

Abstract. Rare earth elements (REEs) are in high demand due to their application in renewable technologies and electromobility. Particular exploration focus is on clay-hosted REE deposits, which typically have a higher proportion of heavy REEs (e.g. terbium and dysprosium) relative to light REEs, which enhance high-temperature properties of permanent magnets. Academic studies have focussed on clay-hosted REE deposits in China, and little is known about the mineralogy and viability of clay-hosted REE projects in Australia. In this study, we: 1) examine the deportment of REEs within clay horizons along with the degree of weathering, 2) contrast relict primary REE minerals with secondary REE minerals formed in the weathering horizon, and 3) quantify the clay mineralogy of various Australian clay-hosted REE projects. The outcomes of this microcharacterisation study illustrate the unique mineralogy of REE clay deposits and indicate the extent to which REEs may be recoverable from the clay horizons.

1 Introduction

Clay-hosted REE deposits, also termed regolith-hosted REE deposits, are mined in the Jiangxi, Guangdong, Fujian, Hunan, Guangxi and Yunnan provinces in South China, and in Malaysia. The deposits are typically formed on ridges during weathering of REE-bearing Cretaceous-to-Jurassic volcanic and granitic rocks. The REE content of the clay horizon may increase up to five times relative to the underlying source rock (Bao and Zhao 2008; Foley and Ayuso 2015). Rare earth elements are released from the underlying magmatic rocks from primary REE host minerals such as allanite, apatite, monazite, titanite, bastnaesite, synchysite, fluorite, or xenotime (Li et al. 2017). During the breakdown of primary host minerals, the REEs may be adsorbed onto the surface of clay minerals such as kaolinite, halloysite, illite, smectite, or vermiculite to form ionic clay-hosted mineralisation (Mukai et al. 2020). In this style of deposit the REEs can be extracted via ionic solutions that preferentially scavenge the REEs but do not dissolve the clay minerals.

The proportion of REEs adsorbed to clay minerals compared to those trapped within acid-resistant, REE-bearing, minerals (e.g. monazite) is a critical factor in determining the economic viability of a REE clay project. Various microcharacterisation studies have been published on prominent clay hosted deposits in China and Madagascar (e.g. Borst et al. 2020); however, little is known about the plethora of clay-hosted REE deposits in Australia.

Current price fluctuations, focus on critical minerals, risk of disrupted supply chains, and governmental support have recently triggered intense exploration efforts for clay-hosted REE mineralisation in Australia, with >50 projects being pursued by junior exploration companies. The information provided in company reports typically relates to the distribution of REEs within the clay horizon from aircore drilling results. However, little is known about the REE mineralogy, which is crucial in identifying the economic potential of clay-hosted REE deposits.

This talk will focus on scanning electron microscopy (SEM) and whole-rock geochemistry results of clay and bedrock from multiple Australian REE clay projects, which assists in identifying their individual mineralogical signatures and secondary/primary REE minerals.

## 2 Methods

2.1 SEM analysis

A thin layer of clay material was smeared onto carbon tape and outgassed for 48 hours in the vacuum chamber of a Quorum Q 150TE plus carbon coater prior to carbon coating. Rock-chip and selected clay samples were either mounted in 30 mm epoxy rounds or prepared as thin sections and analysed using a Zeiss Axiolab 5 petrographic microscope.

Analyses via SEM were performed using a Hitachi SU3900 with two Bruker XFlash 6160 energy-dispersive spectroscopy (EDS) detectors. Backscatter electron (BSE) and secondary electron (SE) images are collected of smear samples using a low acceleration voltage (5–10 keV) and a short working distance (~6 mm).

2.2 Geochemical analysis

The geochemical analysis technique utilised in clay-hosted REE projects is dependent on the individual exploration company and commercial laboratory. Samples typically are from air core, reverse circulation, or sonic drilling. Most available datasets are 4-acid digest multi-element suite, which includes the total REE suite. However this technique may not dissolve acid-resistate REE-bearing phosphate minerals and therefore does not reliably indicate the samples total REE content. In contrast, borate Fusion techniques are also applied as a standard method for analysing the REE content of a sample and includes REE within acid resistate minerals.

For selected projects, early metallurgical test work is presented using ionic solutions (e.g. ammonium sulphate at pH 4), which can be compared to 4-acid or flux-fusion data.
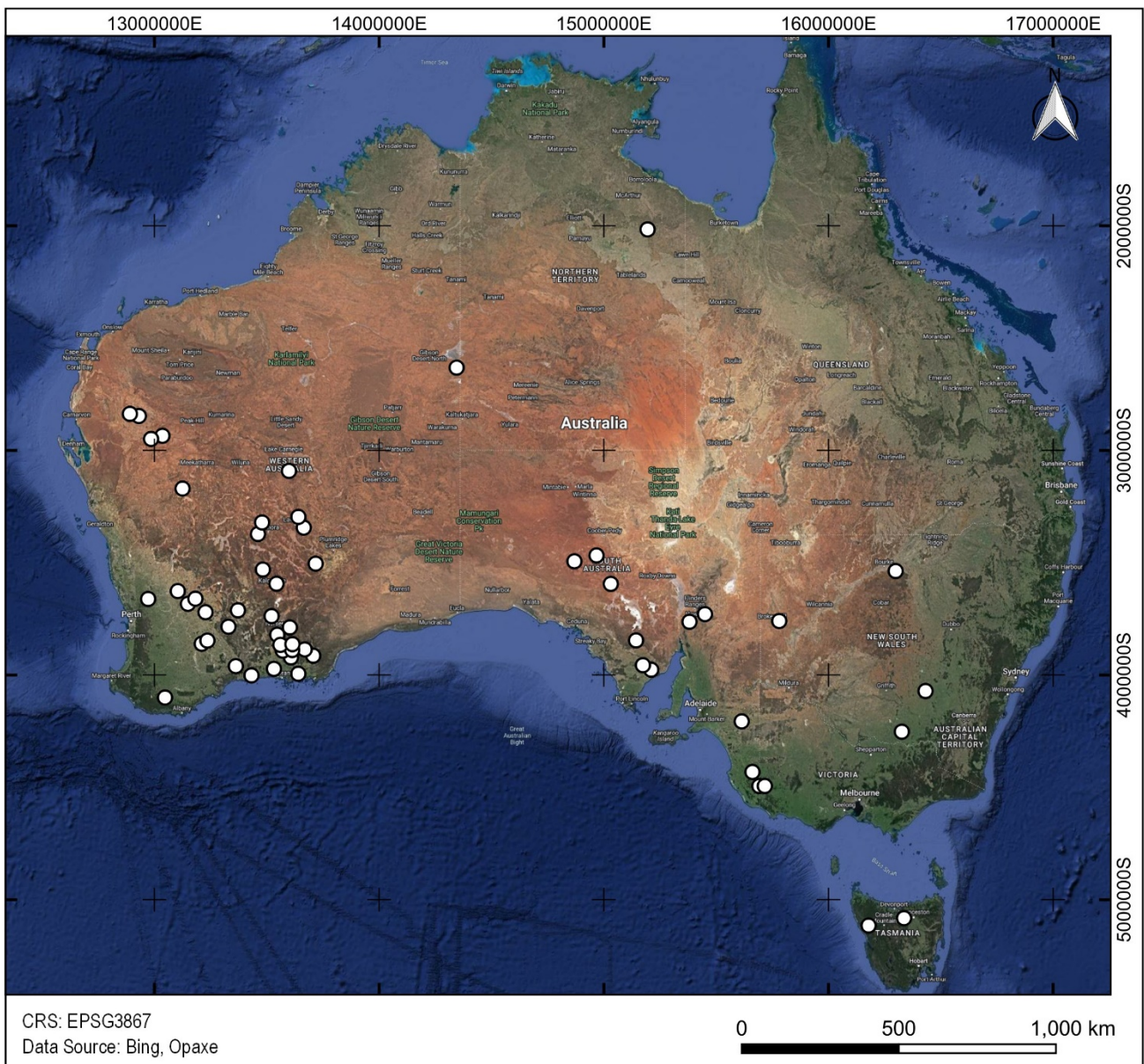
Figure 1: Overview of >50 active rare earth clay projects in Australia, including but not limited to ABx Group, Ardea Resources, Asra Minerals, Auric Mining, Auroch Minerals, Ausmon Resources, Australian Rare Earths, Castillo Copper, ChemX Materials, Desert Metals, Dundas Minerals, Emetals, EMU NL, Forrestania Resources, Godolphin Resources, Golden Mile Resources, Heavy Rare Earths, Horizon Minerals, Indiana Resources, Investigator Resources, iTech Minerals, Kingfisher Mining, Krakatoa Resources, Krakatoa Resources, Lanthanein Resources, Latin Resources, Magnetic Resources, Mamba Exploration, Marmota, Marquee Resources, Meeka Metals, Miramar Resources, Mount Ridley Mines, Moho Resources, Mt Monger Resources, Narryer Metals, Norwest Minerals, OD6, Petratherm, Pursuit Minerals, Resource Base, Sky Metals, Summit Minerals, Tambourah Metals, Taruga Minerals, Terrain Minerals, Traka Resources, Transition Minerals, Venus Metals, Venture Minerals, Victory Goldfield, Voltaic Strategic Resources, West Cobar Metals, and White Cliff Minerals.

3 Results and Discussion

3.1 Overview

A review of exploration activity identified 56 clay-hosted REE projects (Figure 1). Data compiled focused on Australian Stock Exchange (ASX) listed exploration companies and the actual number of projects is expected to be larger. The majority of REE projects (39) are within Western Australia, located in areas with granitic bedrock in the Albany-Fraser Orogen and central Yilgarn Craton. Another cluster is within the Delamerian Orogen and Gawler Craton within South Australia. Almost all clay-hosted REE discoveries in Australia were made within the last three years and information on mineralogy is scarce.

3.2 Primary REE Minerals

Primary REE minerals identified in the SEM study of various REE clay projects include allanite, apatite, Ca-REE fluorocarbonates, fluorite, monazite, titanite, and zircon. These primary magmatic minerals were identified within granitic source rocks that have been partially weathered. Allanite is the dominant primary REE mineral in granitic source
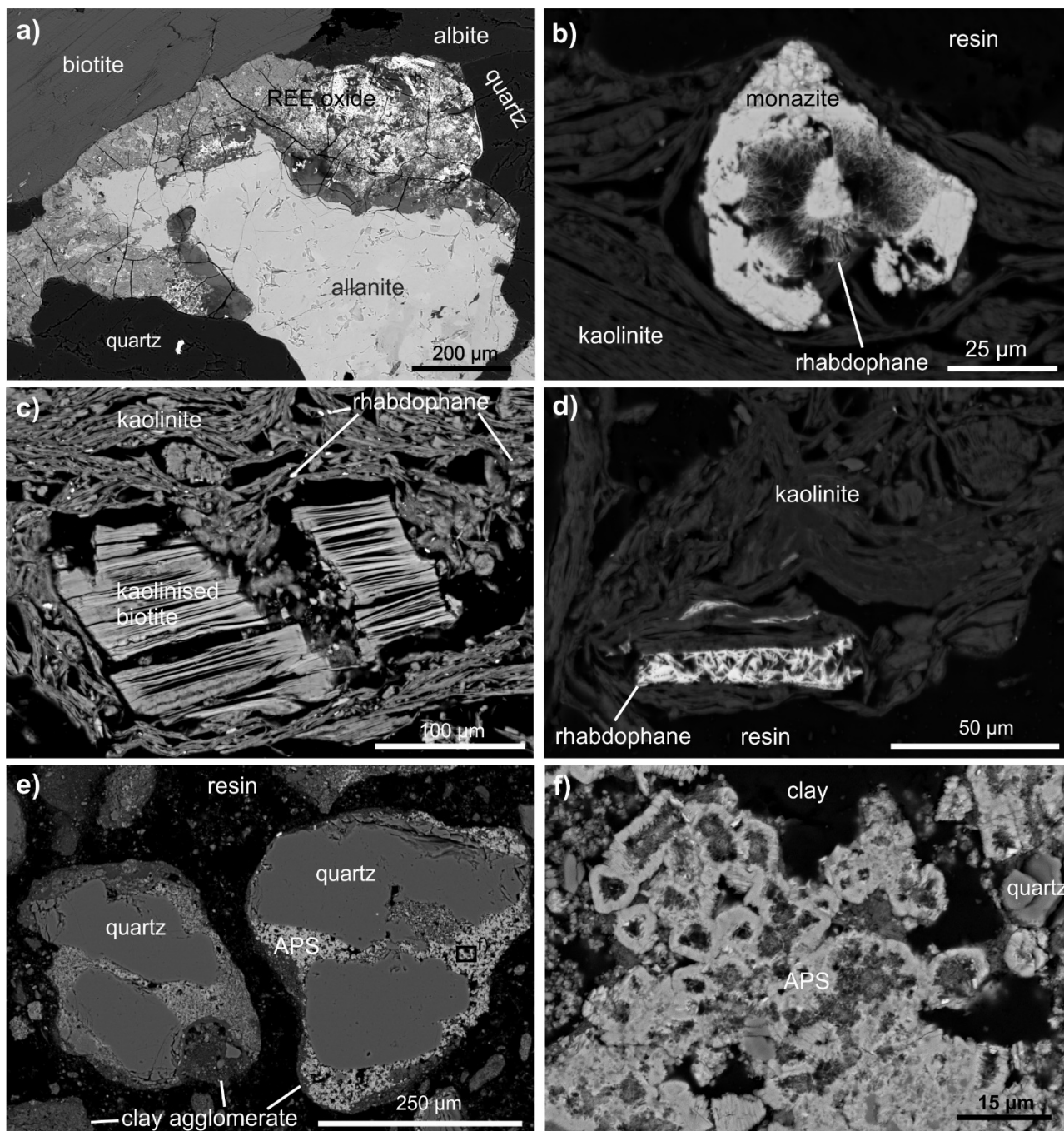
Figure 2: Primary and secondary REE mineralogy in selected Australian REE clay deposits. a) Breakdown of allanite to various Fe and REE oxides in monzogranite; b) Relict monazite in the clay horizon with overgrowth of acicular rhabdophane; c) kaolinite with exfoliated biotite. Note the minute rhabdophane aggregates within kaolinite; d) fibrous rhabdophane growing within kaolinite sheets; e–f) REE-Ba-Ca-bearing Aluminium Phosphate Sulphate minerals (APS) growing in atoll texture around dissolved quartz grains.

rock at one project, and is partially weathered to a complex assemblage Fe/REE (oxyhydr)oxides (Figure 2a). Notably, allanite is the least stable mineral during weathering in the sample in Figure 2a and readily releases REEs during weathering to the clay horizon.

The loss on ignition (LOI) at 1100 °C is typically >8.75 wt.% in fully weathered kaolinite-halloysite horizons (Du Plessis et al. 2021) and can be used as a proxy for the degree of weathering. Clay samples with LOI ≈ 4–5 wt.% contain abundant relict quartz and primary REE minerals both as liberated minerals or inclusions within quartz. In some instances,

primary, granular, monazite with rounded corners (e.g. Schulz 2021) remains intact, suggesting that (some) REEs have not been mobilised during weathering and are locked within primary magmatic minerals such as monazite.

3.3 Secondary REE Minerals

In other instances, monazite is partially dissolved and secondary acicular REE phosphates are observed nucleating on monazite (Figure 2b). The secondary phase is likely rhabdophane [REE(PO$_4$) ·

nH$_2$O] which precipitates during the breakdown of monazite.

Rhabdophane is abundant in the clay horizon of multiple REE clay projects and hosts a portion of the REE content, which is not adsorbed onto the surface on clay minerals. Rhabdophane also grows in needle-like aggregates within kaolinite layers at various size fractions (Figure 2c–d). In contrast to the replacement texture observed in Figure 2b, this textural variety of rhabdophane is not directly related to the breakdown of monazite.

Some exotic REE minerals are also present in clay hosted REE mineralisation. One studied project contains abundant REE-Ba-Ca-bearing Aluminium Phosphate Sulphate minerals of variable composition that are likely attributed to the plumbogummite subgroup of the alunite supergroup, that includes florencite [REEAl$_3$(PO$_4$)$_2$(OH)$_6$], crandallite [CaAl$_3$(PO$_4$)(PO$_3$OH)(OH)$_6$], or gorceixite [BaAl$_3$(PO$_4$)(PO$_3$OH)(OH)$_6$]. These phosphate minerals crystallise in atoll like textures enveloping weathered quartz grains (Figure 2e–f).

4 Conclusion

Rare earth clay projects in Australia are abundant within Archean Cratons within Western Australia and South Australia. Most projects are in their infancy, and it is yet to be determined which prospects host economic, extractable quantities of REEs. Microcharacterisation of REE projects is crucial to identifying primary and secondary REE minerals, which may not be recovered using ionic solutions, as well as clay mineralogy, the degree of weathering and the presence of deleterious minerals. Each prospect analysed in this study is unique in terms of the above-mentioned parameters and therefore may require unique processing techniques for REE extraction.

References

Bao Z, and Zhao Z (2008) Geochemistry of mineralization with exchangeable REY in the weathering crusts of granitic rocks in South China. Ore Geol Rev, 33:519–535. https://doi.org/10.1016/j.oregeorev.2007.03.005

Borst AM, Smith MP, Finch AA, Estrade G, Villanova-de-Benavent C, Nason P, Marquis E, Horsburgh NJ, Goodenough KM, Xu C, Kynický J, and Geraki K (2020) Adsorption of rare earth elements in regolith-hosted clay deposits. Nat Comm, 11:4386. https://doi.org/10.1038/s41467-020-17801-5

Du Plessis PI, Gazley MF, Tay SL, Trunfull EF, Knorsch M, Branch T, and Fourie LF (2021) Quantification of Kaolinite and Halloysite Using Machine Learning from FTIR, XRF, and Brightness Data. Minerals, 11:1350. https://doi.org/10.3390/min11121350

Foley N, and Ayuso R (2015) REE enrichment in granite-derived regolith deposits of the Southeastern United States: Prospective source rocks and accumulation processes. British Columbia Geol Survey Paper 3:131-138.

Li YHM, Zhao WW, and Zhou M-F (2017) Nature of parent rocks, mineralization styles and ore genesis of regolith-hosted REE deposits in South China: an integrated genetic model. J Asian Earth Sci, 148:65–95. https://doi.org/10.1016/j.jseaes.2017.08.004

Mukai H, Kon Y, Sanematsu K, Takahashi Y, and Ito M (2020) Microscopic analyses of weathered granite in ion-adsorption rare earth deposit of Jianxi Province, China. Sci Rep, 10:20194. https://doi.org/10.1038/s41598-020-76981-8

Schulz B (2021) Monazite Microstructures and Their Interpretation in Petrochronology. Front Earth Sci, 9:668566. https://doi.org/10.3389/feart.2021.668566

Zinc incorporation into carbonate minerals from the Selac area, Kosovo

Konrad Kluza[1], Jaroslav Pršek[1], Sławomir Mederski[1], Zdeněk Dolníček[2], Jiří Sejkora[2]
[1] AGH University of Science and Technology, Kraków, Poland
[2] Department of Mineralogy and Petrology, National Museum, Prague, Czech Republic

Abstract. Chemical composition of carbonate minerals from the Selac area in Kosovo was studied. Samples from three sampling areas were analysed by using transmitted-light microscopy and electron microprobe. The main hydrothermal vein mineral is dolomite, which is characterized by enrichments in ZnO (up to 7.2 wt.%) and FeO (up to 12.78 wt.%). Another carbonate minerals found in veins: calcite, magnesite, and siderite are also characterized by zinc incorporation. Two substitutional trends are observed in the Selac dolomites: Fe+Mn enrichment as well as Zn enrichment both substituting Mg.

1 Introduction

Zinc in the nature forms a variety of its own minerals included sulfides, sulfates, oxides, carbonates, phosphates, and silicates, but can also substitute into other minerals (Barak and Helmke 1993). Historically, zinc was mined from non-sulfide deposits (where smithsonite and hemimorphite are the main ore minerals), but over time and the development of processing methods, sulfide deposits rich in sphalerite have become the main source of zinc on the market. However, in recent years there has been a trend in the market to return to exploration and exploitation of non-sulfide zinc deposits, which, moreover, results in the presence of new research on this type of deposits, as well as the processes responsible for their formation (Boni and Mondillo 2015). Hitzman et al. (2003) distinguish two major subtypes of non-sulfide zinc deposits: supergene (related to oxidation of sulfide–type deposits) and hypogene (associated with silicates and zinc oxides).

Carbonates are minerals widely spread in nature and common in different environments (sedimentary basins and hydrothermal environment). One of the well-known member is dolomite $CaMg(CO_3)_2$, which can be primary in various environments (including hydrothermal), but can also be formed by dolomitization of pre-existing carbonate rocks. During dolomitization secondary porosity is generated, one of the key factors for origin of MVT and carbonate-replacement Zn-Pb deposits. In addition, it has a major impact on younger processes linked to later supergene processes responsible for the formation of non-sulfide deposits (Boni et al. 2011). Dolomite could easily incorporate various elements as Mn, Fe, and Zn.

The phenomenon of dedolomitization described by Fairbridge (1978) provides the recrystallization of dolomite to calcite as a result of weathering. Boni et al. (2011) describes the phenomenon of 'zincization' as the incorporation of Zn in dolomite, followed by the formation of smithsonite, in the context of supergene non-sulfide deposits.

2 Geology

The Selac area is located in the northern part of Kosovo, near the famous Pb-Zn-Ag Stan Terg deposit. That area is a part of the Trepça Mineral Belt, which is main metallogenic belt in Kosovo and belongs to bigger suture zone named Vardar Zone (Fig. 1). Mineralization and alterations in that area have hydrothermal origin and are related to Oligocene-Miocene volcanic activity (Strmić Palinkaš et al. 2013).
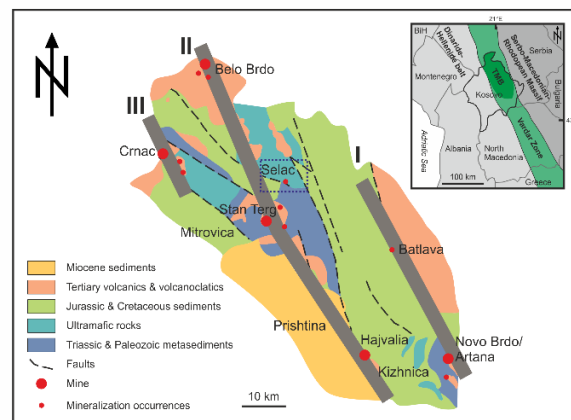
Figure 1. Geological map of Trepça Mineral Belt, Kosovo (modified after Strmić Palinkaš et al. 2013; Mederski et al. 2021) with marked study area. I – Batlava – Artana zone, II – Belo Brdo - Stan Terg -Hajvalia zone, III – Crnac zone.

Lithologies in the Selac area are represented mainly by Jurassic ultrabasic rocks and serpentinites which occurs together with ophiolite and mélange with small amount of Paleozoic crystalline basement (formed by schist and phyllites) with intensive Tertiary unit represented by volcanics, sub-volcanic intrusive and pyroclastic rocks (Mederski et al. 2021). On the border between serpentinites and volcanic rocks, as well as in tectonic zones hydrothermally altered rocks - listvenites occur. Listvenites often host hydrothermal mineralization (Mederski et al. 2021).

Mineralogy of the studied listvenites and hydrothermal veins consists of carbonates (dolomite, magnesite), quartz, chalcedony, and fuchsite. Ore mineralization is represented by galena, sphalerite, nickeline, maucherite, gersdorffite, rammelsbergite, polydymite, marcasite, pyrite, millerite, and chromite (Mederski et al. 2021).

Dolomite N = 316		Oxide in wt. %											
		MgO	P₂O₅	CaO	MnO	PbO	FeO	ZnO	CoO	NiO	CuO	Al₂O₃	BaO
SL_I N = 29	Minimum	15.82	0.04	27.32	0.06	b.d.l.	1.03	b.d.l.	b.d.l.	0.08	b.d.l.	0.03	b.d.l.
	Maximum	22.64	0.18	30.25	0.36	b.d.l.	9.92	b.d.l.	b.d.l.	0.21	b.d.l.	0.30	b.d.l.
	Median	20.27	0.11	29.22	0.17	b.d.l.	3.99	b.d.l.	b.d.l.	0.14	b.d.l.	0.05	b.d.l.
SL_II N = 254	Minimum	11.84	0.01	16.10	0.05	0.13	0.09	0.14	0.06	0.07	b.d.l.	0.03	b.d.l.
	Maximum	23.40	0.63	31.80	1.00	1.16	11.12	7.20	0.13	12.92	b.d.l.	1.88	b.d.l.
	Median	17.82	0.08	28.26	0.20	0.26	5.41	1.28	0.08	0.12	b.d.l.	0.06	b.d.l.
SL_III N = 33	Minimum	9.66	0.01	21.19	0.08	0.19	0.10	0.20	0.01	0.12	0.01	0.03	0.01
	Maximum	19.16	0.16	29.20	0.68	12.43	12.78	7.16	0.05	0.45	0.09	0.50	0.09
	Median	15.05	0.08	28.32	0.23	0.39	4.49	1.10	0.02	0.21	0.04	0.15	0.03
Calcite N = 9	Minimum	0.23	0.03	37.08	0.05	0.31	0.16	0.19	0.01	0.09	b.d.l.	0.04	0.03
	Maximum	7.28	0.44	57.56	0.48	7.63	6.61	3.10	0.01	0.09	b.d.l.	0.07	0.25
	Median	0.52	0.04	51.60	0.09	2.25	0.39	1.07	0.01	0.09	b.d.l.	0.06	0.03
Magnesite N = 15	Minimum	15.93	0.03	0.03	0.05	0.19	3.57	1.44	0.10	0.08	b.d.l.	0.03	b.d.l.
	Maximum	47.67	0.05	10.07	0.43	0.19	23.30	14.61	0.10	1.74	b.d.l.	0.07	b.d.l.
	Median	33.88	0.04	0.22	0.23	0.19	13.40	6.36	0.10	0.13	b.d.l.	0.05	b.d.l.
Siderite N = 2	Minimum	14.62	0.00	0.42	0.49	b.d.l.	28.59	1.65	0.08	0.52	b.d.l.	b.d.l.	b.d.l.
	Maximum	14.74	0.00	0.70	0.93	b.d.l.	36.99	11.55	0.08	0.95	b.d.l.	b.d.l.	b.d.l.
	Median	14.68	0.00	0.56	0.71	b.d.l.	32.79	6.60	0.08	0.74	b.d.l.	b.d.l.	b.d.l.

Table 1. Chemical composition of carbonates from Selac area; b.d.l. = below detection limit.

3 Methods

3.1 Investigated material

Representative samples of dolomite vein were collected from the outcrops surrounding the village Selac in Kosovo. Samples comes from massive dolomite veins and with macroscopically visible nickel arsenide crystals. Sample area has 1.5 km width (Fig. 2), where three outcrops in the same tectonic zone were investigated. Sample location Sl_I is the most easterly. Rock samples are strongly carbonated and silicified with a lot of carbonates or silica veins; breccia also occurs. Sample location SL_II is the most westerly sample point. Rock samples are collected from coarse-crystalline carbonate vein. Dolomite veins with visible zonality was found. Sample location Sl_III is located near the Selac village. Samples are strongly silicified with visible carbonate vein and Ni mineralization; breccia is also found.
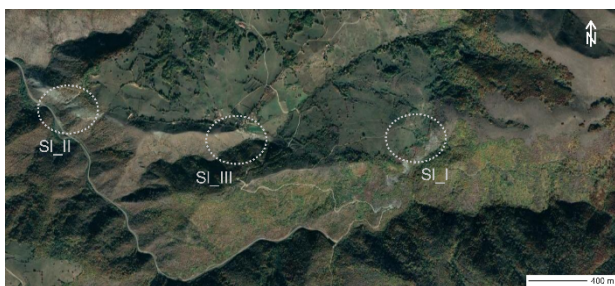

Figure 2. Map of the Selac area with marked sample spots.

3.2 Analytical techniques

Preliminary petrographic investigation of carbonates from the Selac area was conducted in transmitted-light microscopy. Chemical analyses of representative ore samples were determined by a Cameca SX100 electron microprobe (EPMA) at the Department of Mineralogy and Petrology, National Museum in Prague. Operating conditions were an accelerating voltage of 15 kV, a beam current 5, 8, 10 nA, peak time of 20 sec, and a background time of 10 sec. Natural and synthetic standards were used. The natural standards were: diopside, wollastonite, rhodonite, celestite, wulfenite, haematite, barite, fluoroapatite, chalcopyrite, sanidine, whereas the synthetic standards were ZnO, Co. Spectral lines MgKα, PKα, SiKα, CaKα, MnKα, SKα, SrLβ, PbMα, FeKα, ZnKα, CoKα, NiKα, CuKα, AlKα, BaLα were used for analyses.
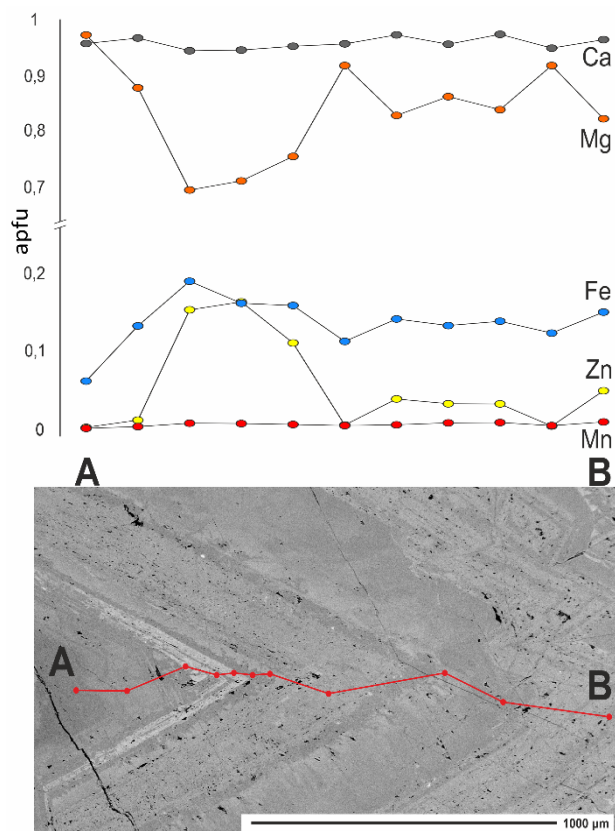

Figure 3. Oscillatory zoned dolomite crystal from Selac. Brighter zones are enriched in Fe and Zn, and depleted in Mg.

4 Results

4.1 Dolomite

Dolomite occurs mostly in crystal forms with a wide range of crystal size (from few μm up to few mm). They are showing a specific crystal structure – enormous amount of chipping visible in transmitted-light microscopy which are arranged perpendicular to the crystallization directions of the crystals. Moreover, they create zones which are better visible by using SEM. Zonation in that area are caused by varying metal content – Mg, Fe, Mn, Zn. Two zone types in dolomite are recognized. Firstly, oscillatory Fe-Mn rich zones without or with low amount of Zn and secondly, irregular zones with high Fe and Zn content (Fig.3, Fig.4).

Generally, dolomite from the Selac is characterized by relatively constant CaO content and enrichments in Fe, Mn, Zn, Pb and Ni on magnesium position.

Dolomite from SI_I is characterized by MgO content between the 15.8 to 22.6 wt.%, while average content of CaO is equal to 29.2 wt.%. It is worth to notice that enrichment in FeO is up to 9.9 wt.%. Additionally, there is no enrichment in ZnO observed here (Tab.1).

Dolomite from SI_II and SI_III shows some similarities. Content of MgO in SI_II varies from 11.8 to 23.4 wt.% and in SL_III between 9.7 and 19.2 wt.%. Average content of CaO is similar: 28.2 wt.% in SI_II and 27.7 wt.% in SI_III. Dolomites from these areas show the presence of Fe and Zn. Median of FeO content is 5.41 wt.% in SI_II and 4.5 wt.% in SI_III, whereas median of ZnO content is 1.3 wt.% in SI_II and 1.1 wt.% in SI_III. Additionally, some dolomite zones from the SI_III are characterized by the unusual PbO enrichment in maximum up to 12.4 wt.%, (with median equals 0.4 wt.%), while some dolomite zones from the SI_II show NiO enrichment (up to 12.9 wt.%, and median equals 0.1 wt.%) (Tab.1).

4.2 Other carbonates

Other minor carbonates are represented mostly by calcite, zoned and brecciated magnesite, and rarely siderite. Calcite mostly forms the small veinlets and sometimes overgrow dolomite crystals. Magnesite and siderite build host rock (serpentinite) and they occur in massive form or as a relict in quartz/dolomite veinlets (Fig.4).

Composition of calcite shows enrichment of MgO (up to 7.3 wt.%), PbO (up to 7.6 wt.%), FeO (up to 6.6 wt.%) and ZnO (up to 3.1 wt.%) (Tab.1). Magnesite is characterized by wide range of MgO (15.9-47.7 wt.%) and FeO (3.6-23.3 wt.%), there are also visible enrichment in ZnO up to 14.6 wt.% and rarely increased amount of CaO (up to 10.1 wt.%) (Tab.1). Siderite is characterized by FeO content between 28.6 wt.% and 37.0 wt.% and MgO content which median is equal 14.68 wt.%. In siderite is

visible increased content of ZnO, which median is 6.6 wt.%. (Tab.1).
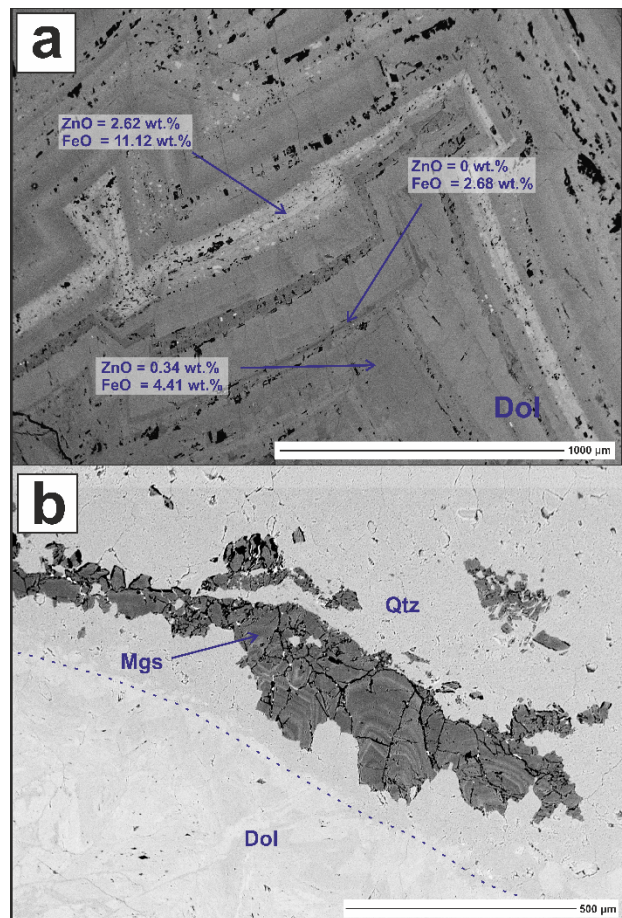
Figure 4. BSE images, **a** - dolomite crystal with oscillatory zones; **b** - Magnesite relict in quartz-dolomite vein.

5 Discussion

Observation of the textures, as well as the chemical composition of the carbonates from the Selac dolomite vein indicates the multi-stage formation of these veins. Breccias, overgrown textures and zonations (oscillatory and irregular), suggest variable crystallization conditions. In addition, two major substitutional trends are observed that reflect the processes responsible for vein formation in Selac (Fig.5).

Firstly, primary - oscillatory zonation in dolomite crystals can be a result of $(Fe^{2+} + Mn^{2+}) \leftrightarrow Mg^{2+}$ substitution (which is observed mainly in SI_I) may have the hydrothermal origin, what is common in Kosovo and TMB, where the occurrence of Mn in carbonate minerals is typical in many hydrothermal localities (Mederski et al. 2021)

Secondly, irregular zonation characterized by perpendicular to crystal borders chipping, may be as a result of $Zn^{2+} \leftrightarrow Mg^{2+}$, what has been so far described by Boni et al. (2011) as a dedolomitization phenomenon in dolomite mineral. Together with supergene alteration of Zn-Pb sulfide ores it results in formation of nonsulfide deposits.
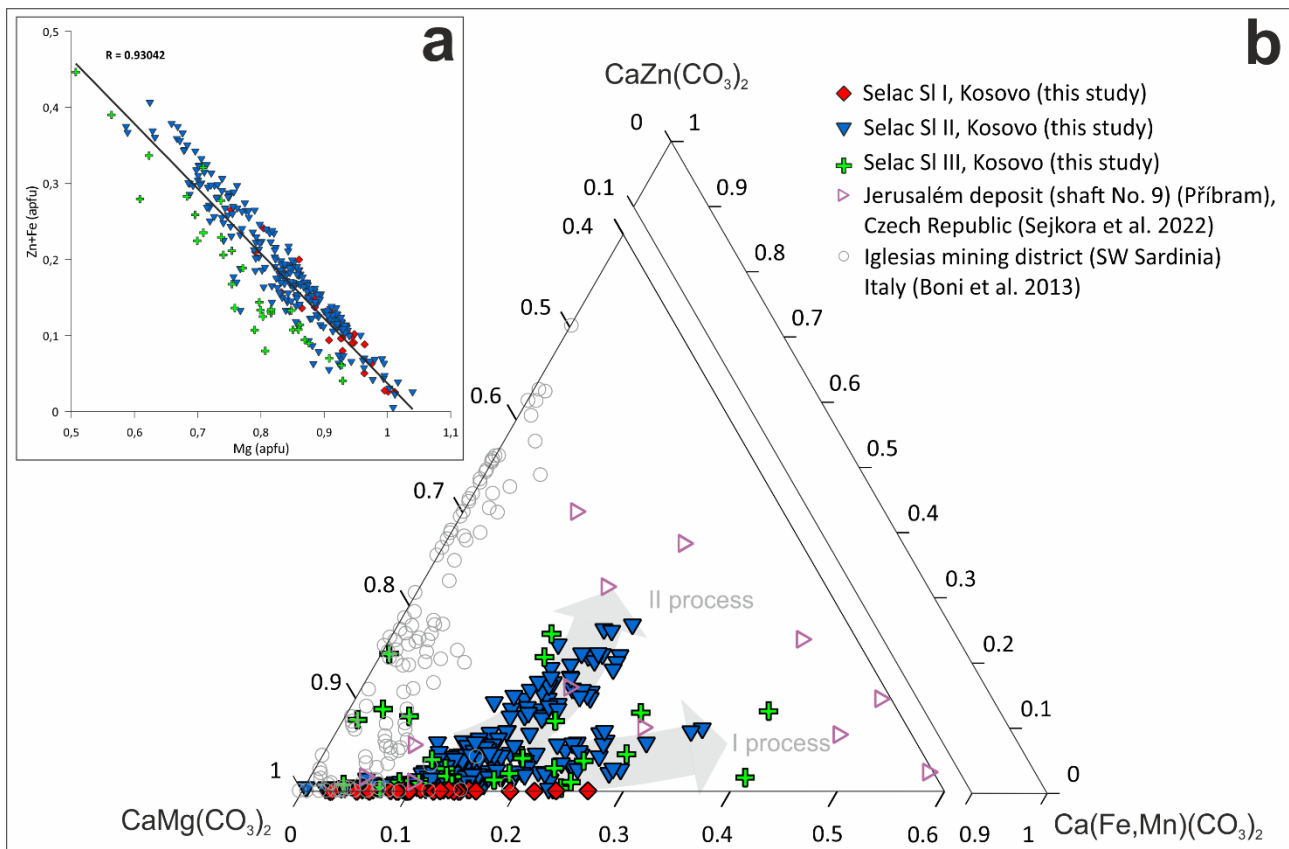
Figure 5. a - Plot of Zn+Fe substitution instead of Mg (in apfu); **b -** Composition of dolomites from Selac area in the system $CaMg(CO_3)_2 – Ca(Fe,Mn)(CO_3)_2 – CaZn(CO_3)_2$, with comparison of data from Boni et al. 2013 and Sejkora et al. 2022.

On the other hand, Sejkora et al. (2022) described Zn-enriched dolomites of hydrothermal origin from the Jerusalém deposit from the Příbram uranium and base-metal district (Czech Republic). Zn rich dolomites from this locality are also rich in Mn and Fe and occur in paragenesis with quartz, siderite, willemite, Cu arsenides, or Cu-Ag sulfides. The formation temperatures of this paragenesis, depending on the thermometer used, range from 70 to 136 °C (Sejkora et al. 2022).

A similar situation is found at Selac, where Zn-rich dolomite occurs in paragenesis with arsenide (Ni) association and is suspected to be of hydrothermal origin. Probably, the presence of Zn in dolomites from Selac is due to low sulfur activity in hydrothermal fluids. This fact is mentioned by Mederski et al. (2021), who referred to the above conditions for the formation of arsenide Ni association, as well as gersdorffite with a high As/S ratio. Confirmation of the potential low temperatures of this unique association in Selac requires further fluid inclusion studies.

Acknowledgements

References

Barak P, Helmke PA (1993) The Chemistry of Zinc. Part of the Developments in Plant and Soil Sciences book series (DPSS 55)

Boni M, Mondillo N (2015) The "Calamines" and the "Others": The great family of supergene nonsulfide zinc ores. Ore Geol Rev 67:208-233

Boni M, Mondillo N, Balassone G, Joachimski M, Colella A (2013) Zincian dolomite related to supergene alteration in the Iglesias mining district (SW Sardinia). Int J Earth Sci 102:61-71

Boni M, Mondillo N, Balassone G, (2011) Zincian dolomite: A peculiar dedolomitization case? Geology 39/2:183-186

Fairbridge, RW (1978) Dedolomitization. The encyclopedia of sedimentology. 233–235

Hitzman MW, Reynolds NA, Sangster DF, Allen CR, Carman CE (2003) Classification, Genesis and Exploration Guides for Nonsulfide Zinc Deposits. Econ Geol 98: 685-714

Hyseni S, Durmishaj B, Fetahaj B, Shala F, Berisha A, Large D (2010) Trepça Ore Belt and Stan Terg mine – Geological overview and interpretation, Kosovo (SE Europe). Geologija 53/1:87-92

Mederski S, Wojsław M, Pršek J, Majzlan J, Kiefer S, Asllani B (2021) A geochemical study of gersdorffite from the Trepça Mineral Belt, Vardar Zone, Kosovo. J Geosci 66:97-115

Sejkora J, Dolníček Z, Škácha P, Ulmanová J, Vrtiška L (2022) Unusual mineralization with willemite from the area of the central part of the Příbram uranium and base-metal district (Czech Republic). Bull Mineral Petrolog 20/2:224-242

Strmić Palinkaš S, Palinkaš LA, Renac Ch, Spangenberg JE, Lüders V, Molnar F, Maliqi G (2013) Metallogenic Model of the Trepça Pb-Zn-Ag Skarn Deposit, Kosovo: Evidence from Fluid Inclusions, Rare Earth Elements, and Stable Isotope Data. Econ Geol 108:135-162

Germanium mineralization in subbituminous coal from the Sokolov Basin, Czech Republic: The origin and volatility of Ge

Kříbek B[1], Rohovec J[2], Bičáková O[3], Tuhý M[1,4], Sýkorová I[3], Straka P[3] Pticen F[1], Vymazalová A[1] Poňavič M[1]
[1]Czech Geological Survey, Geologická 6, 152 00 Prague 5, Czech Republic
[2]Institute of Geology, Academy of Sciences of the Czech Republic, Rozvojová 269, 165 00 Prague 6, Czech Republic
[3]Institute of Rock Structure and Mechanics, Czech Academy of Sciences, V Holešovičkách 41, 182 09 Prague 8, Czech Republic
[4]Institute of Geochemistry, Mineralogy and Mineral Resources, Faculty of Science, Charles University, Albertov 6, 128 00 Prague 2, Czech Republic

Abstract. Miocene subbituminous coal (ortho-lignite) from the Sokolov coal basin (Ohře Graben, Czech Republic) contains up to 400 ppm Ge. However, the regional distribution of Ge in the studied Antonín and Josef coal seams is highly variable. The highest Ge concentrations are confined to the interface between the coal seams and the crystalline basement. Germanium in coal is bound mostly to pyritized coal macerals. The origin of Ge mineralization is explained by the infiltration of Ge-bearing solutions during the weathering of crystalline rocks and/or hydrothermal activity along the border faults of the coal basin. In calcination or gasification of coal, Ge was released in a vapour phase at temperatures of 780 to 810 °C. Very high Ge concentrations (up to 8,380 ppm) were found in fly ash.

1 Introduction

The continental Ohře (Eger) Graben (Czech Republic) hosts the Most, Sokolov and Cheb basins, filled with thick Paleogene to Pliocene siliciclastic sediments and coal seams (Rojík et al., 2014; Fig. 1a). In the Sokolov basin (Fig. 1b), the Antonín and Anežka coal seams are developed in Miocene sedimentary units, and the underlying Josef Seam in Oligocene sediments. All seams are relatively high in sulphur and arsenic. The main objective of this study was to study the areal distribution and binding of Ge in the Antonín and Josef seams and to assess the volatility of Ge during coal calcination or gasification as a prerequisite for the possibility of industrial germanium production.

2 Materials and Methods

To evaluate the distribution of Ge in the Antonín and Josef seams, 26 samples were collected from the individual technological position of the seams. Samples were dried, crushed and calcined to temperature of 200, 500, 700 900 and 1100 °C in the laboratory furnace. The thermodesorption (TD) analysis of the coal sample was performed using the setup introduced by Tuhý et al. (2021). It consists of a combustion unit (Clasic CZ, Czech Republic) connected at the outlet to an ICP-OES plasma torch (Iris Intrepid II XSP ICP-OES; Thermo-Scientific, USA; Fig. 2). The device operates under a continuous argon flow. The samples were heated from 25 °C to 900 °C with a linear gradient of 50 °C per minute. The elements of interest (As, Ge, Hg and S) were continuously and simultaneously detected (at analytical lines of 189.0 nm, 206.8 nm, 184.9 nm and 182.0 nm, respectively). The gasification of a constant weight coal sample was performed in the gasification unit (Fig. 3). The coal sample was heated to the temperature of 900 °C.
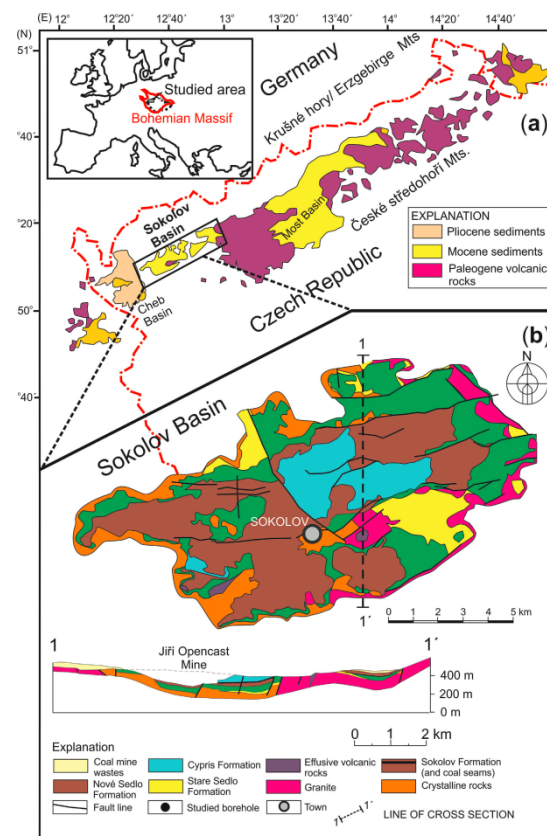
Figure 1. A geological sketch map of the Ohře Graben (**a**); modified after Matys Grygar and Mach (2013), and detailed map of the Sokolov Basin (**b**) (after Rojík et al. 2014).
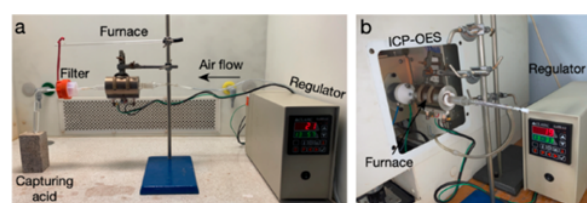
Figure 2. Thermodesorption of Ge, As, Hg and S was performed using coal combustion in a glass reactor (**a**). The coal sample was heated to a temperature of 1200 °C and the concentrations of elements in a gas phase were continuously monitored by an emission spectrometer with inductively coupled plasma (**b**).
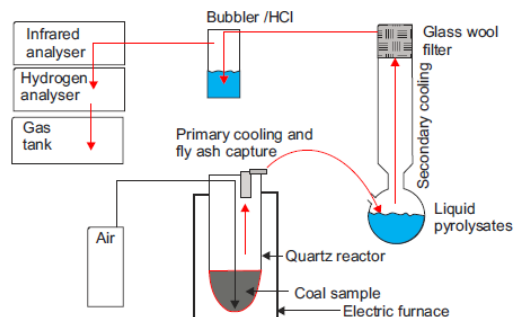
Figure 3. A simplified scheme of the laboratory pyrolysis unit. Unit drivers were omitted.

3 Results and Discussion

2.1 Germanium mineralization in coal

The concentrations of Ge and other selected elements in the Antonín and Josef coal seams are given in Table 1. Low Ge concentrations were found in coal of the central part of the basin, while high Ge contents (up to 380 ppm) were found only in its peripheral part, along the contact with the underlying Krušné hory Crystalline rocks (Fig. 4).

Table 1. Concentrations of Ge and other selected elements in the marginal and central part of the Antonín and Josef coal seems (Sokolov Basin, Czech Republic). Concentrations of C_{org} and S_{tot} are given in wt.%, those of Cu, Ge, As and Mo in ppm, those of Hg in ppb. n= 26.

|	Cu	Ge	As	Mo	Hg	C_{org}	S_{tot}
Antonín and Josef seams, peripheral part of the Sokolov basin, contact with the crystalline basement							
Max.	7	411	41	12.3	20	43.2	6.8
Average	9	396	39	11.3	12	46.6	5.9
Min.	11	350	390	10.3	80	378	4.5
Antonín and Josef seams, central part of the Sokolov basin							
Max.	190	13.7	31	9.82	12	61.1	7.4
Average	81	5.52	164	7.69	8	54.9	5.1
Min.	25	1.11	37	3.55	10	51.4	1.7

The high contents of Ge in the marginal part of the seams can be explained by its introduction during weathering of the mineralized crystalline basement and/or hydrothermal activity along the marginal faults. The same mechanism has been reported by Dai et al. (2014) in the study of Ge mineralization of the Lincang deposit in the Yunnan region, NW China. Dai et al. consider the mineralization to be epigenetic.

Germanium-rich coal consists mainly of macerals of the huminite group (55 – 63 vol.%). It is dominated by completely gelled ulminite (24 – 27 vol.%), followed by textinite (remnants of cell structures) and attrinite. Macerals of the liptinite and fusinite groups are less common and do not contain Ge. The inorganic components are dominated by clay minerals, pyrite and quartz (Havelcová et al., 2015). Germanium is dispersed in the mass of fully gelled ulminite but is particularly concentrated in strongly pyritized textinite. This is confirmed by the good correlation between the distributions of Ge and S (Fig. 5).
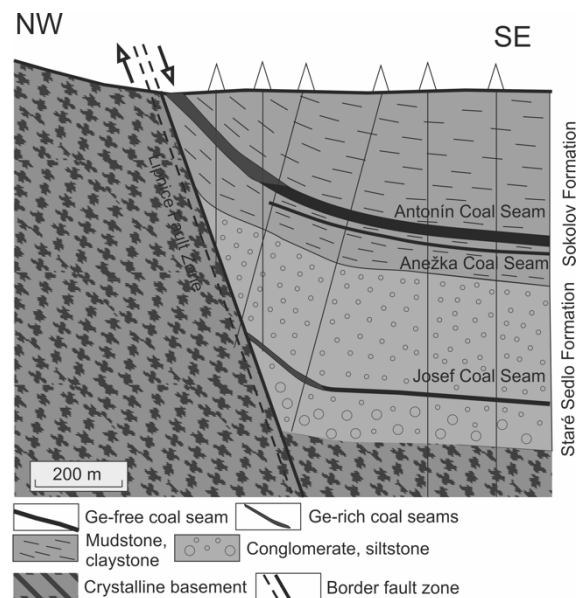
Figure 4. Geological position of high Ge contents in the Antonín and Josef seams in the Sokolov Basin. Elevated Ge contents are bound only to seams that closely adjoin the tectonically strongly affected rocks of the underlying crystalline unit. Germanium concentrations in the seams in the central part of the basin are very low (Table 1). Not to scale.
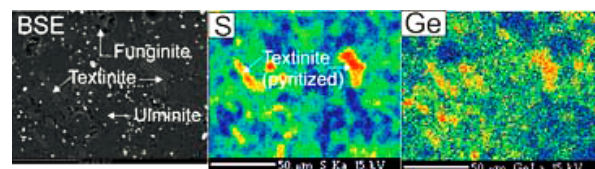

Figure 5. The distribution of S and Ge in coal of the Antonín Seam. Germanium is dispersed in ulminite but the highest Ge contents are bound to pyritized fragments of porous textinite.

3.2 Calcination of coal

During the calcination of coal samples with high Ge contents in a laboratory oven, the concentrations of Ge and other "volatile" elements were found to generally increase at lower temperatures and then

gradually decrease, due to their volatilization. The concentrations of Ge in coal ash, for example, gradually increase up to the temperature of 700 °C but rapidly decrease at higher temperatures (Fig. 6). At the calcination temperature of 700 °C, the concentration of Ge was found to increase from 420 ppm (in the original coal) to 1180 ppm in the calcinated coal residuum.
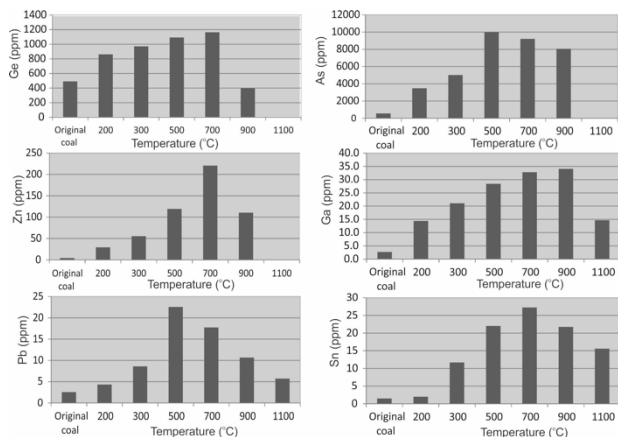

Figure 6. Concentrations of Ge and other volatile elements in calcinated coal residuum at temperatures in the range of 200 to 1100 °C. The Antonín Coal seam, sample HU 28/2022.

The highest concentrations of Ge (0.8 to 1.2 wt.%) were found in irregular clusters of hematite, whose morphology resembles pyritized particles of organic macerals, especially textinite (Fig. 7a, Fig. 8). In contrast, globular formations of hematite whose morphology resembles early diagenetic framboidal pyrite (Fig. 7b) are Ge-free. This suggests that the formation of Ge-rich coal is not linked to the early diagenetic stage of organic matter development, when framboidal pyrite is usually formed, but to the late diagenetic or epigenetic stages of seam evolution, and is associated with pyritization of porous organic remains.
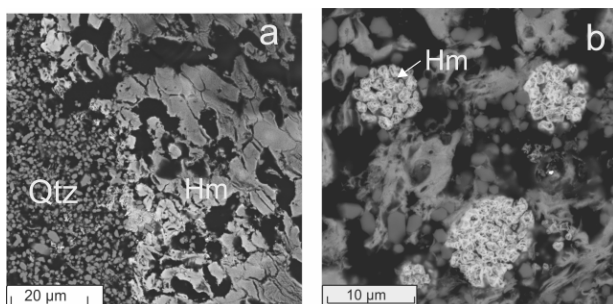
Figure 7. Two morphological types of hematite in coal after calcination at 700 °C. **a**: Porous hematite aggregates (Hm) are interpreted as an oxidation product of the pyritized coal fragment. This type of hematite aggregates shows Ge contents of max. 1.2 wt.%. **b**: Globular form of hematite aggregates, probably representing an oxidative product of pyrite framboids. Germanium was not detected in this morphological type of hematite. Qtz: authigenic quartz grains.

Figure 8. Distribrution of Fe (b) and Ge (c) in porous hematite cluster in the calcination residuum whose
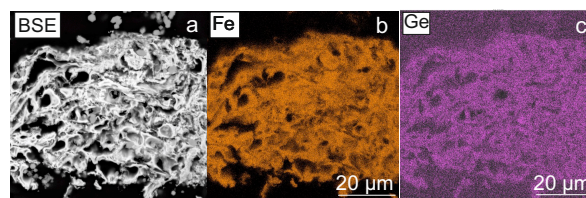
morphology resembles pyritized particles of organic macerals. Back scattered electrons (BSU).

3.3 Continuous monitoring of the Ge, S, Hg and As thermodesorption

Simultaneous volatilization of S, Hg and As occurred initially at temperatures around 350 °C, suggesting their similar speciation most probably in sulphides/sulphosalts. Maximum As release was observed at around 600 °C, followed by a sharp decrease. Germanium started to mobilize at temperatures of >700 °C and showed a single discrete peak at 800 °C (Fig. 9). This corresponds to the results of coal calcination in a laboratory furnace (Fig. 6).
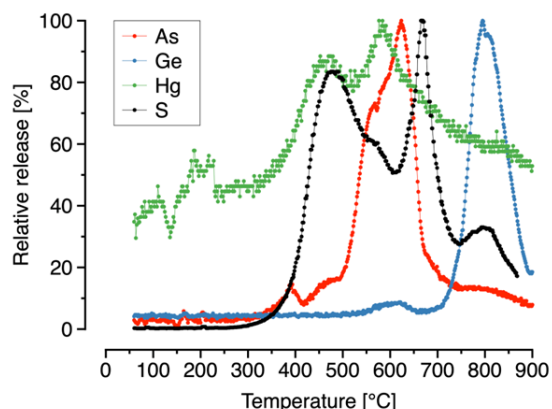
Figure 9. Relative release of elements from a coal sample (G21) as a function of temperature obtained by a combustion-simulating setup with a continuous temperature increase and online ICP-OES detection. For a better comparison of the individual curves, data were normalized to the maximum peak.

3.4 Gasification of coal at the temperature of 900 °C.

The previous experiments revealed that the thermodesorption of Ge occurs at temperature around 800 °C. In order to achieve complete gasification of Ge, coal samples were gasified at a quartz reactor, at the temperature of 900 °C. Due to exothermic character of the coal gasification, the temperature inside the sample increased and fluctuated between 910 and 950 °C and was monitored by a thermocouple in the coal sample. The simplified scheme of the gasification apparatus is shown in Figure 3. Experiment was carried out in duplicate.

The concentration of Ge and other elements were recorded in an original coal sample, in a solid coal residue after thermal treatment, in a primary cooling unit where flay ash was collected, in liquid

pyrolysate, glass wool filters and in bubbler filled with 0.5 M HCl (Fig.3).

Compared to original coal (average concentration of Ge: 134 ppm; Table 2), the concentration of Ge in the coal residue in the reactor was below the detection limit of the analytical method used (XRF) (Table 2).

The highest concentrations of Ge were recorded in fly ash (average Ge concentration: 8,380 ppm) and in filters (3,072 ppm). The results of the powder X-ray diffraction showed that the fly ash consists of a large amount of amorphous aluminosilicates, quartz and small amount of anatase (TiO_2). Of the Ge compounds, GeO_2 (trigonal variety) and GeS (orthorhombic variety) were identified. This indicates that Ge in fly ash is bound to solid particles. However, it cannot be ruled out that a part of Ge is binded by sorption to other components of the system, especially to amorphous aluminosilicates or to hematite.

The Ge concentrations in a liquid gasification product were very low and ranged between 64.2 in liquid pyrolysate and 2.99 ppm in a bubbler filled with 0.5 M HCl (Table 2).

Table 2. Average concentrations of Ge, As and Hg during gasification of brown coal samples at a temperature of 900 °C ($n = 2$).

Substrate	Ge	As	Hg
Coal sample before gasification	134	870	<LOD
Coal sample after gasification (coal solid residuum)	<LOD	1042	<LOD
Fly ash	8,380	10,522	2,200
Liquid pyrolysate	64.2	30.5	0.735
Glass wool filter	3,072	3,595	614
Bubbler / 0.5 M HCl	2.99	3.11	1.23

4 Conclusions

Germanium mineralization in the Sokolov Basin is restricted to the contact of the coal seams with the crystalline basement. In the central part of the basin, Ge concentrations are very low. This suggests that the source of Ge can be seen either in low-temperature weathering of crystalline rocks or in a hydrothermal activity associated with movements along border faults of the sedimentary basin. Germanium in coal is dispersed in gelified coal organic matter. However, the highest Ge concentration was recorded in pyritized fragments of porous coal macerals. On the other hand, Ge was not recorded in framboidal pyrite, which was formed during the early diagenesis of coal seams. This confirms that the Ge ore mineralization is confined to the late diagenetic or epigenetic stages of the development of coal seams.

During the calcination of coal, Ge concentrations in the ash gradually increase up to a temperature of 700 °C. At this temperature, Ge in the calcinated coal residuum is mainly bound to hematite, which is formed during pyrite oxidation. The concentrations of Ge in hematite reach max. 1.2 wt.%. At higher temperatures, Ge concentrations sharply decrease.

Continuous monitoring of the thermodesorption confirmed that Ge is volatilized at ~800 °C. In contrast, a significant part of potentially harmful elements (S, As and Hg) are released at lower temperatures. The observed differences in the volatility of Ge S, As and Hg allow us to consider the separation of Ge and more volatile elements at different gasification temperatures.

During the laboratory gasification of coal in a quartz reactor at a temperature of 900 °C, the highest concentrations of Ge were found to be bound to fly ash or to glass wool filters. In the fly ash, Ge was present in the form of GeO_2 and GeS. The presence of GeS indicates a reaction between $Ge_{(vapour)}$ and $S_{(vapour)}$ during the gasification. The amount of Ge in the liquid gasification product was very low. This indicates that the fly ash captured on dry or water filters at high temperatures of coal gasification or combustion and subsequent Ge extraction with acids (HCl, H_2SO_4) or organic extractants can be an effective method of industrial Ge recovery.

References

Dai S, Wang P, Colin R.W, Tang Y. Song X, Jiahuna J, Hower JC, Li T, Seredin V, Wagner NJ, Yaofa J, Wang X, Liu J (2014) Elemental and mineralogical anomalies in the coal-hosted Ge ore deposit of Lincang, Yunnan, southwestern China: Key role of N_2–CO_2-mixed hydrothermal solutions. Int J Coal Geol 152:19–46.

Havelcová M, Sýkorová I, Mach K, Trejtnarová H, Blažek J (2015) Petrology and organic geochemistry of the lower Miocene lacustrine sediments (Most Basin, Eger Graben, Czech Republic). Int J Coal Geol 139:26–39.

Matys Grygar T, Mach K (2012) Regional chemostratigraphic key horizons in the macrofossil-barren siliciclastic lower Miocene lacustrine sediments (Most Basin, Eger Graben, Czech Republic). Bulletin of Geosciences 88:557–571.

Rojík P, Dašková J, Kvaček Z, Pešek J, Sýkorová I, Teodoridis V (2014) The Sokolov Basin. *In*: Pešek J (ed.) *Tertiary Basins and Lignite Deposits of the Czech Republic*. Czech Geol Survey, Prague, pp 90–142.

Tuhý M, Ettler V, Rohovec J, Matoušková Š, Mihaljevič M, Kříbek B, Mapani B (2021) Metal(loid)s remobilization and mineralogical transformations in smelter-polluted savanna soils under simulated wildfire conditions. J Environmental Management 293:112899.

Weathering processes associated to the formation of supergene Cu-As-Pb-Zn minerals at the Cap Garonne mine (France, Provence)

Julien Poot[1], Johan Yans[1], Gaëtan Rochez[1], Pierre Buelens[2], Augustin Dekoninck[2]
[1]University of Namur, Department of Geology, Institute of Life-Earth-Environment, Namur, Belgium
[2]Université Libre de Bruxelles, Laboratoire G-Time, Département Géosciences, Environnement et Société, Brussels, Belgium

Abstract. The Cap Garonne mine hosts more than 150 minerals (16 of them are type-locality) with a large part related to supergene processes. Primary mineralization mostly consists of tennantite [$(Cu,Zn,Ag,Fe)_{12}As_4S_{13}$] and galena [$PbS$] in a few-meters thick Permo-Triassic (P-Tr) fluviatile conglomerate. The secondary mineralization is very diverse and mainly consists in a succession of covellite [CuS], olivenite [$Cu_2(AsO_4)(OH)$], brochantite [$Cu_4(SO_4)(OH)_6$] and anglesite [$PbSO_4$] , cerussite [$PbCO_3$], malachite [$Cu_2(CO_3)(OH)_2$], and azurite [$Cu_3(CO_3)_2(OH)_2$]. The acidic fluids generated by the oxidation of primary sulfides led to the formation of secondary sulfides and some arsenates. The further neutralization processes, mostly by the calcite contained in the cement of the host conglomerate, allowed the precipitation of arsenates, sulfates and carbonates.

1 Introduction

The Cap Garonne old mine is located SW of the Maures Massif and S of the Permian Depression in the Toulon-Cuers Basin. The Cu-Pb-As-Zn mineralization contains a rich mineralogical assemblage of more than 150 species including 16 type-locality (Favreau et al. 2014 and personal comm. of the AAMCG). Most of them are micromineralization (e.g.

galeaclolusite [$Al_6(AsO_4)_3(OH)_9(H_2O)_4]\cdot 8H_2O$]) (Grey et al. 2021). The primary mineralization is mostly represented by tennantite and galena, with some occurrences of chalcopyrite, rarely sphalerite and pyrite (Chiappero 1993; Guillemin 1952). Secondary sulfides are limited to chalcocite, digenite and covellite. Secondary minerals cover a wide range among sulfates, carbonates and arsenates. The mining site is separated in two blocks by an E-W vertical fault (Figure 1A) with the southern mine hosting Cu-As mineralization (Figure 1B), while the northern mine mainly consists in Cu-As-Pb(-Zn) mineralization (Figure 1C). The first written records of the Cap Garonne mines date back to the 17th century, although the first mining license was not granted until the mid-19th century. The mines were never continuously exploited and were closed in 1917 after about 30 years of exploitation, mainly due to the fluctuation of copper price and other new deposit types with better grades. During this period, 30,000 tons of Cu ore (5 wt. %) and 500 tons of Pb ore (7-16 wt. %) were produced (Favreau et al. 2014).
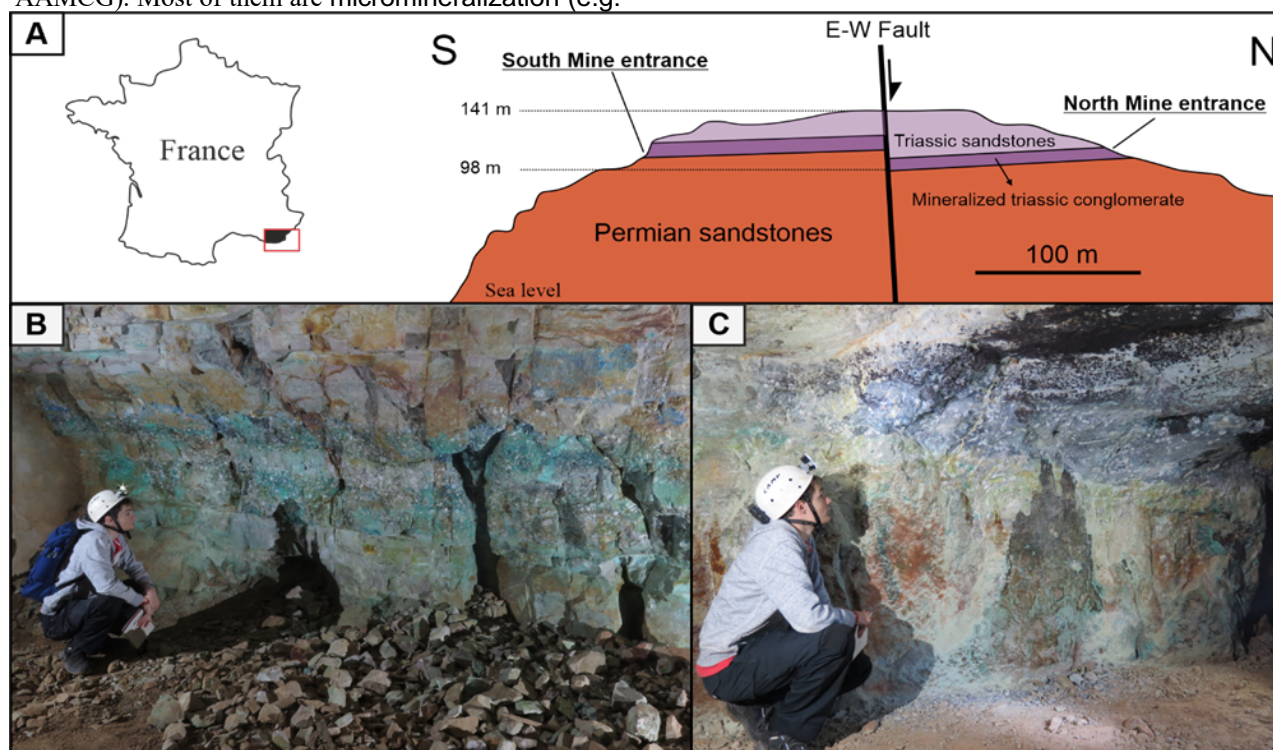
Figure 1. (A) Location and geological section of the Cap Garonne mine (modified from Guillemin 1952; Favreau et al. 2014). (B) Southern mine. (C) Northern mine.

2 Methodology

Most samples were collected from both sides of the Cap Garonne old mine. Permian and Triassic host rocks mostly come from the Colle Noire Massif. The analyses used to study these samples include X-ray diffraction (XRD), whole rock (46 samples) geochemistry (major, minor and trace elements), scanning electron microscopy (SEM), transmission and reflection light microscopy.

3 Results

3.1 Host (fresh) rocks

P-Tr transition rocks consist of sandstones, siltstones and several lenses of conglomerate with (pluri)centimetric quartz pebbles. The fresh Early Triassic conglomerate (Port-Issol Fm.) locally hosts the Cap Garonne mineralization and shows a carbonate cement. The overlying reddish Permian sandstone and the entire sandy Triassic sequence have a decreasing carbonate content compared to the P-Tr conglomerate. Carbonates, mostly calcite, also occur as veins and cm-size geodes in Permian rocks. Major mineral phases observed in these host rocks are quartz, muscovite, calcite, feldspars and barite.
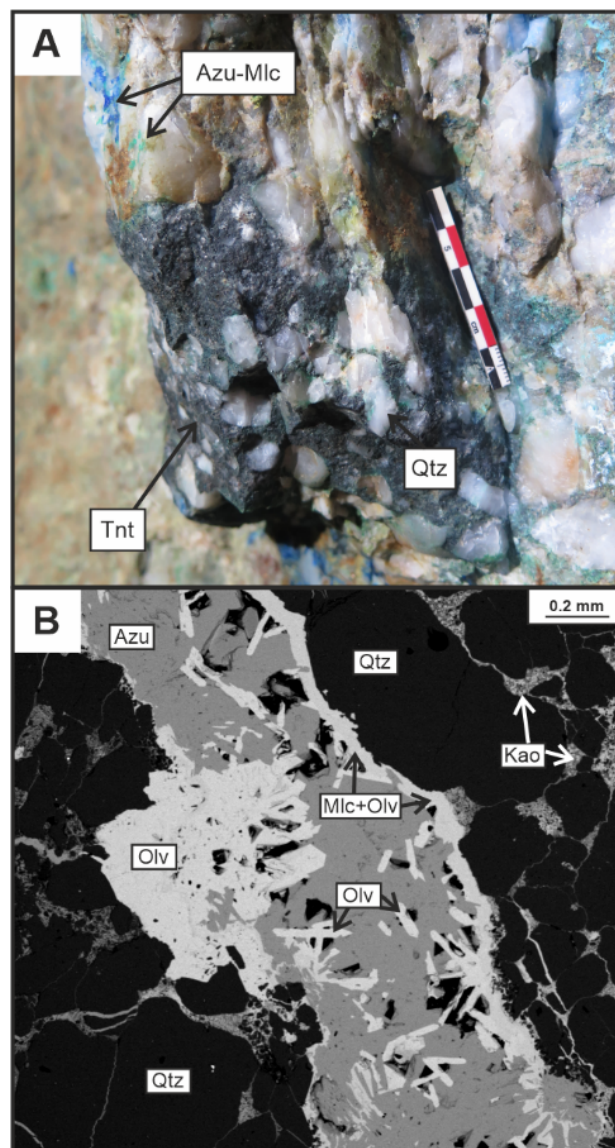
3.2 Southern mine

The southern mine exposes Cu-As mineralization with tennantite as the most abundant primary sulfide, mostly in the conglomerate and generally associated with malachite and azurite (Figure 2A). Secondary mineralization is observed as incrustation and stratabound fill in (micro)fractures (Figure 2B) or within the intergranular volume of the rock.

Secondary copper sulfides phases are digenite [Cu_9S_5], chalcocite [Cu_2S], covellite, djurleite [$Cu_{31}S_{16}$], generally surrounding tennantite. Other minerals such as mansfieldite [$AlAsO_4.2H_2O$] antlerite [$Cu_3(SO_4)(OH)_4$] brochantite, pharmacoalumite [$KAl_4(AsO4)_3(OH)_4.6.5H_2O$], (arseno)gorceixite [$BaAl_3(AsO_4,PO_4)_2(OH)_5.H_2O$], camerolaïte [$Cu_4Al_2(HSbO_4,SO_4)(CO_3)(OH)_{10}.2H_2O$] and barite are also observed. Olivenite can be observed in tennantite, with small concretions of cornwallite or cornubite (polymorphs of [$Cu_5(AsO_4)_2(OH)_4$]) or even associated with malachite and azurite veins (Figure 2B). Pluri-centimetric clay levels can also be observed in the galleries and often contain azurite veins and pebbles.

3.3 Northern mine

The north mine includes both Pb-Zn and Cu-As mineralization (Figure 3). The layout of the mineralization is the same as to the southern mine.

Galena and sphalerite also are primary sulfides in addition to tennantite. Rare Co- and Ni-bearing sulfides can also be observed such as gersdorffite or Ni-rich cobaltite [$(Ni,Co)AsS$]. Secondary mineralization is also directly associated with primary sulfides and is made of anglesite, mimetite [$Pb_5(AsO_4)_3Cl$] and other Cu-As minerals observed also in the southern mine. Most Pb-Cu arsenates (Figure 3) are recognized as thin crusts close to the Pb zone. Rare erythrite [$Co_3(AsO_4)_2.8H_2O$] is identified in Co-bearing pocket, as micromineralization. Iron oxides are observed as crusts or veins filling generally intersecting the Cu-As-Pb-Zn mineralization.

Figure 2. (A) Tennantite (Tnt) and azurite-malachite (Azu-Mlc) mineralization in P-Tr conglomerate, southern mine. (B) SEM microphotographs of mineralized vein of azurite, olivenite (Olv) and malachite, with small veins fill of kaolinite (Kao).
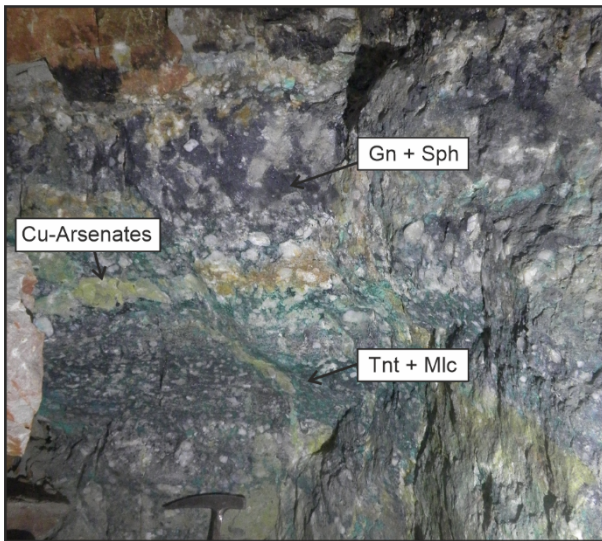
Figure 3. Association of Cu-As and Pb-Zn mineralization in north mine (Gn = Galena, Sph = Sphalerite).

4 Weathering processes

4.1 Paragenesis

The paragenetic sequence for the Cu-As zone is sulfides I → sulfides II → arsenates (Cu-depleted) → Cu-arsenates → sulfates → carbonates. The oxidation of tennantite with O_2-rich meteoric water allows the formation of secondary Cu-sulfides surrounding the primary sulfide. Cu-depleted arsenates such as mansfieldite, arsenogorceixite or pharmacoalumite are formed after sulfides II and prior to Cu-arsenates filling, such as olivenite (Figure 4). This suggests that early arsenates incorporate cations from the host rocks (K, Ba, Al, Fe), instead of Cu, at this point crystallized as secondary sulfides. Olivenite precipitation occurs under less acidic and more oxidizing conditions, which involves a neutralization of acidic fluids with in-situ phyllosilicates. With tennantite still being oxidized, olivenite formation leads to an excess of Cu^{2+} in solution and allows local precipitation of secondary Cu arsenates, such as cornubite or cornwallite located between tennantite and olivenite. Accumulation of sulfate potentially leads to the precipitation of brochantite or antlerite after the first neutralization episode. Finally, dissolution of the carbonated cement in the fluids completely neutralizes the system, and precipitates malachite and azurite in the mineralized levels as a result.

Regarding the Pb-Zn zone, the paragenetic sequence is quite similar but quite simpler. Galena oxidizes into an anglesite matrix which is stable under a wide range of pH and Eh. This prevents further oxidation of galena and sphalerite. The neutralization by carbonate also allows the formation of cerussite. However, as few Zn supergene mineralisation (e.g. adamite $[Zn_2AsO_4(OH)]$) is observed, it is suggested that Zn is located as substitution in Cu secondary minerals.
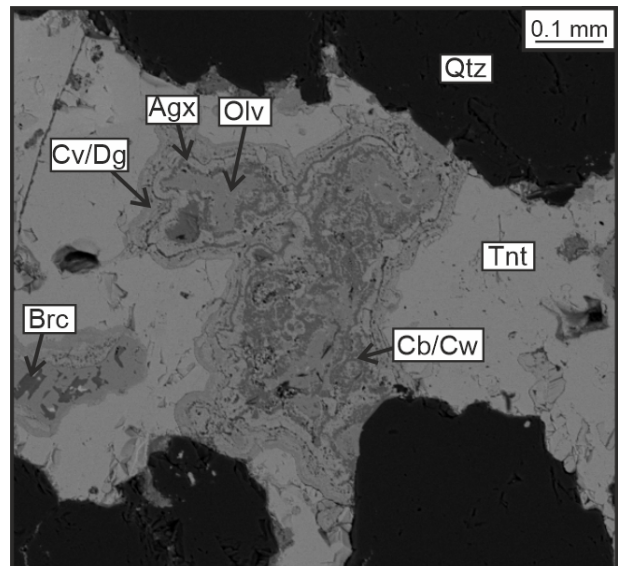
Figure 4. SEM microphotographs with tennantite and associated weathering phases (Cb/Cw = cornubite, cornwallite, Agx = arsenogorceixite, Cv/Dg = covellite, digenite).

4.2 Supergene model

At Cap Garonne the Permo-Triassic transition starts with maximum 8m-thick conglomerate intersected by several clay lenses (Durand 2008). Then hydrothermal activity with S-enriched mesothermal fluids allows the formation of two separate levels: the lower level with mostly tennantite while the upper level contains galena with some sphalerite and tennantite. These sulfides could possibly be related to the Permian volcanic activity of the Colle Noire Massif (Vuillet 1995).

Once the protore formed, weathering processes can start with the percolation of meteoric fluids through fractures and porosity. Those fluids lead to oxidation of sulfides and release acidic fluids rich in various metals. This process may be exacerbated by the longer residence time of meteoric fluids due to the presence of clay levels. Secondary minerals then precipitate according to the sequence mentioned in section 4.1, with various patterns in the northern or southern mine. The structural offset between the northern and southern mines (Figure 1), combined with the absence of any Pb-Zn mineralization in the southern mine suggests an initial erosion of the Pb-Zn level south of the E-W fault.

The precise age of the secondary mineralization is difficult to estimate but probably belongs to the major periods of weathering in the area, during early Cretaceous, Eocene and late Oligocene (Hautmann and Lippolt 2000, Dekoninck et al. 2019). However, the deposit is located a few meters below the surface and then ongoing weathering is observed and lead to some new (micro)mineralization.

5 Conclusion

At Cap Garonne the polymetallic character of the protore is at the origin of a very diversified secondary mineralization. Southern mine is characterized by a

Cu-As mineralization while the northern mine also shows Pb-Zn minerals. The mineralization sequences are quite similar in both parts of the mine and show a pattern as follows: (i) sulfides I, (ii) sulfides II, (iii) arsenates, sulfates and sulfo-arsenates, (iv) carbonates. Neutralization process mainly comes from carbonates from the cement of the P-Tr conglomerate. Secondary mineralization occurs in the vicinity of the primary sulfides which supports a very low mobility of the metals and thus reduces the potential environmental issues.

Acknowledgements

References

Chiappero P-J (1993) Les arséniates de cuivre naturels : Systèmatique et approche des conditions de genèse par les synthèses. Applications au gisement plumbocuprifère de Cap Garonne (Var, France). Thèse de doctorat, Université d'Orléans.

Dekoninck A, Monié P, Blockmans S, et al (2019) Genesis and 40Ar/39Ar dating of K-Mn oxides from the Stavelot Massif (Ardenne, Belgium): Insights into Oligocene to Pliocene weathering periods in Western Europe. Ore Geol Rev 115:103191

Durand M (2008) Permian to Triassic continental successions in southern Provence (France): An overview. Boll della Soc Geol Ital 127:697–716.

Favreau G, Galéa-Clolus V, Brun P, Cotte J-P, Bono H, Merlin T, Monniot P (2014) Cap Garonne. Association Française de Microminéralogie, France.

Grey IE, Favreau G, Mills SJ, et al (2021) Galeaclolusite, $[Al_6(AsO_4)_3(OH)_9(H_2O)_4] \cdot 8H_2O$, a new bulachite-related mineral from Cap Garonne, France . Mineral Mag 85:142–148.

Guillemin C (1952) Etude minéralogique et métallogénique du gîte plumbocuprifère du Cap Garonne (Var). Bull la Société française Minéralogie Cristallogr 75:70–160.

Hautmann S, Lippolt HJ (2000) 40Ar/39Ar dating of central European K-Mn oxides - a chronological framework of supergene alteration processes during the Neogene. Chem Geol 170:37–80.

Vuillet J (1995) Etude géologique du Massif de la Colle Noire, à l'Est de Toulon. Université des sciences de Marseille, Marseille.

A hydrous Mg silicate Ni deposit within the oxide type Moa Bay laterite mining district, eastern Cuba

Cristina Villanova-de-Benavent[1], Esperança Tauler[1], Diego Domínguez-Carretero[1], Cristina Domènech[1], Salvador Galí[1], Joaquín A. Proenza[1]
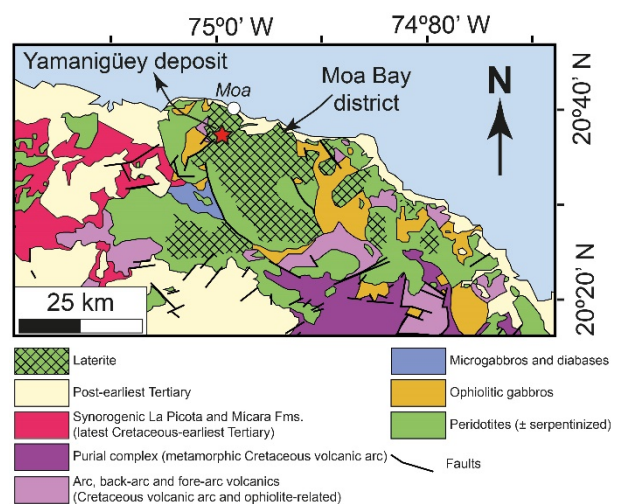*[1]Departament de Mineralogia, Petrologia i Geologia Aplicada, Facultat de Ciències de la Terra, Universitat de Barcelona (UB), Spain*

Abstract. Moa Bay is a world-class Ni laterite mining district with reserve estimates of 53.4 Mt at 1.16 % grade Ni. The vast majority of the deposits belong to the oxide type, and are mined for their Ni-bearing Fe-oxyhydroxides in the oxide zone. One exception is Yamanigüey which can be classified as a hydrous Mg silicate Ni-laterite deposit. The study of a weathering profile of this deposit reveals that it is characterised by a thick saprolite horizon containing secondary Ni-bearing serpentines with 0.6 to 4.8 wt.% NiO, crosscut by garnierite veins. Garnierites from Yamanigüey consist of mixtures between serpentine- and talc-like particles, with 10.9-32.5 wt.% NiO, and Ni being concentrated in the talc-dominant garnierites. The garnierite veins display oscillatory compositional zoning, with lower Mg contents towards the centre of the vein, which may suggest that the precipitation of garnierites is multi-episodic.

1 Introduction

Ni-Co laterite deposits are regoliths formed after chemical and mechanical weathering of ultramafic rocks under tropical and subtropical climates (e.g. Elias 2002). Recently, Ni-laterites surpassed sulphide ores as the main source of Ni, and currently account for 60% of Ni worldwide resources (USGS 2021). The Caribbean area is a major host of Ni-laterite occurrences, and only Cuba represents up to 6% Ni of the worldwide reserves (USGS, 2021). In particular, Eastern Cuba hosts one of the largest Ni-laterite provinces in the world, and includes Moa Bay, Pinares de Mayarí and Nicaro (Lewis et al. 2006 an references therein). Most of the Ni-laterite deposits at the Moa Bay mining district belong to the oxide type (see Brand et al. 1998), but a few present features typical of the hydrous Mg silicate type, one of them being the Yamanigüey deposit (Figure 1). Reserve estimates at Moa Bay are at least 53.4 Mt at 1.16 % Ni, while provable and proven reserves at Yamanigüey are 0.9 Mt at 1.33 % Ni (CSA Global Report Nº R117 2019).

Laterite deposits in Eastern Cuba were first mined in the early 1940s. Since then, different companies, including the Cuban government's state mining company, exploited other concessions around the city of Moa. Nowadays, operations are led by Moa JV (a 50:50 partnership between Sherritt and General Nickel Company S.A. of Cuba). Despite mining activities are focused on the oxide zone, there has been exploration in the saprolite zone since the early 1980s (CSA Global Report Nº R117 2019).

Figure 1. Geological map of the Moa Bay Ni-Co laterite mining district within the Moa-Baracoa massif (Eastern Cuba). The red star marks the location of the Yamanigüey deposit.

The aim of this work is to study the geochemistry, mineralogy, and the Ni distribution across the Ni-bearing phases along a Ni-laterite profile of the hydrous Mg silicate type Yamanigüey deposit.

2 Geological Setting

The Moa Bay Ni-laterites formed after exposure and weathering of the ultramafic rocks of the Cretaceous Mayarí-Baracoa Ophiolite Belt (MBOB; Lewis et al. 2006; Iturralde-Vinent et al. 2016; Proenza et al. 2018) in Eastern Cuba. This ophiolite belt can be divided into two massifs: i) Mayarí Cristal (to the West), and ii) Moa-Baracoa (to the East), neither of them showing a complete ophiolitic sequence (Proenza et al. 1999). The Moa-Baracoa massif is 2.2 km thick, and consists of partly serpentinised harzburgite tectonites with minor dunite. Plagioclase-bearing dunites, wehrlites, lherzolites and pyroxenites have also been described (Marchesi et al., 2006). Interestingly, the Moho transition zone (MTZ) is clearly preserved. The top of the sequence is composed of layered and isotropic gabbros, pillow basalts with a back-arc affinity, chert and limestone; but it is tectonically over-thrusted by the mantle sequence (Proenza et al. 1999, 2006, 2018; Marchesi et al. 2006, 2007).

Laterisation of the Moa Bay serpentinites began in the Miocene and is still ongoing (Lewis et al. 2006 and references therein). Ni-laterite deposits in the

Moa Bay district include Moa Oriental, Moa Occidental, Punta Gorda, Yagrumaje, Camarioca Norte, Camarioca Sur, La Delta, Cantarrana, Santa Teresita, Zona A, Zona Central, Playa la Vaca, Zona Septentrional and Yamanigüey (Lavaut 1998; CSA Global Report Nº R117 2019).

Yamanigüey is part of the Moa Occidental deposit, and is located near the city of Moa (Holguín province), in Eastern Cuba (Figure 1) (Marrero-Leyva et al., 2006). It extends over 1.2 km^2, and is located at 200 masl forming a stepped plateau with altitudes decreasing towards the northeast.

3. Analytical methods

Twenty samples were collected every 50 cm along one 10 m-long profile from Yamanigüey. Whole rock analyses were carried out at Actlabs Laboratories (Ontario, Canada) with the analytical packages "4C-Laterites" (fusion X-ray fluorescence-XRF) and "4-Lithores" (fusion inductively coupled plasma emission mass spectrometry-ICPMS).

X-ray diffraction analyses were performed on a fraction of the samples ground with agate mortar and pestle, in a PANalytical X'Pert PRO MPD Alpha1 powder diffractometer in Bragg-Brentano h/2h geometry of 240 mm of radius, nickel filtered Cu Ka radiation (k = 1.5418 Å), with 45 kV–40 mA and a sample spinning time of 2 revolutions per second. A variable divergence slit kept an area illuminated constant (10 mm), a mask was used to limit the length of the beam to 12 mm, and axial divergence Soller slits of 0.04 radians were used. The samples were scanned from 4 to 80° 2θ with a step size of 0.017° and measuring time of 50 seconds per step, using an X'Celerator detector (active length = 2.122°).

Polished thin sections were prepared and examined under a petrographic polarised light microscope at the Universitat de Barcelona, and using an Environmental Scanning Electron Microscope (SEM) Quanta 200 FEI, XTE 325/D8395 equipped with an INCA Energy 250 Energy Dispersive Spectrometry (EDS) microanalysis system at 20 kV and 5 nA. Finally, quantitative electron microprobe analyses (EMPA) on Ni-bearing minerals were obtained in a JEOL JXA-8230 equipped with five Wavelength Dispersive Spectrometers (WDS), at 15 kV and 15 nA, with a 1-2 μm beam diameter and 10-30 s counting time per element. The standards used were: wollastonite (Si), corundum (Al), orthoclase (K), hematite (Fe), periclase (Mg), rhodonite (Mn), NiO (Ni), metallic Co (Co), rutile (Ti), Cr$_2$O$_3$ (Cr). XRD, SEM and EMPA analyses were carried out at the Centres Científics i Tecnològics of the Universitat de Barcelona (CCiT-UB).

4. Results and discussion

4.1. Whole rock geochemistry

The sampled profile consists of, from the bottom to the top: i) a serpentinised bedrock (8.5-10.0 m), ii) a saprolite zone (3.0-8.5 m), and iii) an oxide zone (0-3.0 m).

The bedrock is a dark green, heavily fractured, massive peridotite with a moderate degree of serpentinisation. It contains 36-39 wt.% SiO$_2$, 37-38 wt.% MgO, 7-8 wt.% Fe$_2$O$_3$, <2 wt.% Al$_2$O$_3$, <1 wt.% MnO, <0.3 wt.% NiO, and 95-110 ppm Co.

The saprolite is a darker green, cohesive rock towards the bedrock that evolves to a dull green softer material towards the top of the horizon. It is crosscut by numerous small silica and garnierite veinlets. Its whole rock composition is 35-42 wt.% SiO$_2$, 30-38 wt.% MgO, 8-13 wt.% Fe$_2$O$_3$, <10 wt.% Al$_2$O$_3$, <1 wt.% MnO, 0.3-3.6 wt.% NiO, and 60-110 ppm Co.

The oxide zone consists of brownish yellow loose material made up of Fe oxyhydroxides with small Mn oxyhydroxide and silica veinlets. This horizon is characterised by remarkable Ni (0.7-2.1 wt.% NiO), and Co contents (up to 0.6 wt.% CoO), and also 36-71 wt.% Fe$_2$O$_3$, 6-38 wt.% Al$_2$O$_3$, <3 wt.% MnO, 1-5 wt.% SiO$_2$, and <2 wt.% MgO.
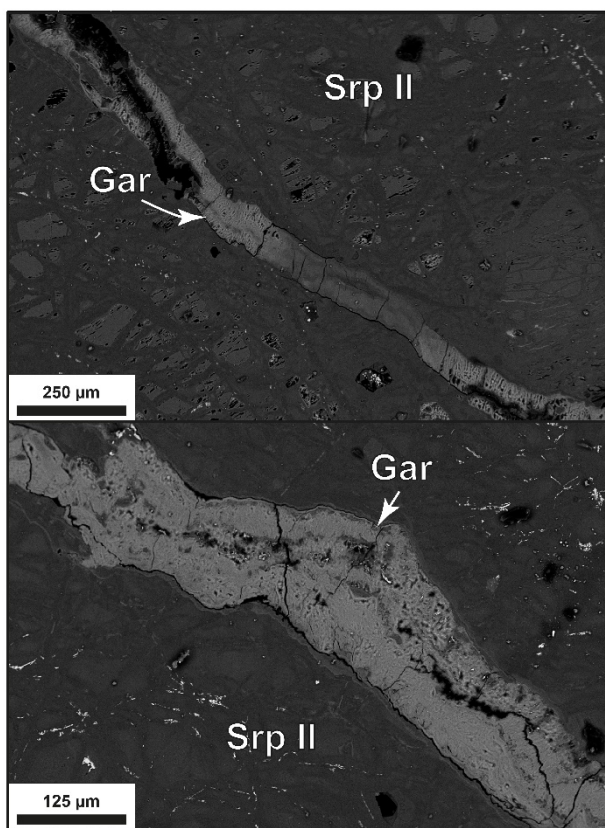
4.2. Mineralogy and petrography of the laterite profile

The bedrock is composed of olivine and minor orthopyroxene, both replaced and/or surrounded by serpentine, with lesser amounts of subhedral Cr-spinel and magnetite. Serpentine yields less than 0.5 wt.% NiO.

The saprolite horizon mainly consists of primary serpentine (Ni-poor, hereafter "serpentine I"), secondary serpentine (Ni-rich, hereafter "serpentine II"), with smaller amounts of magnetite, Cr-spinel, garnierite and Mn-Ni-Co oxyhydroxides. Serpentine is the main constituent, and only a few isolated, rounded relicts of olivine and pyroxene may be found within the serpentine matrix. Serpentine occurs as veins crosscutting the primary bedrock mineralogy (the typical mesh texture in serpentinised ultramafic rocks), and as pseudomorphs of olivine and pyroxene (Figure 2).

It must be noted that serpentine II predominates over serpentine I in the saprolite horizon. The average structural formula of serpentine I from Yamanigüey is Mg$_{2.60}$Fe$_{0.28}$Ni$_{0.01}$Al$_{0.03}$Si$_{2.02}$O$_5$(OH)$_4$, with Ni contents below 0.45 wt.% NiO, and between 3.55 and 12.30 wt.% FeO. In contrast, the average structural formula of serpentine II is Mg$_{2.30}$Fe$_{0.47}$Ni$_{0.08}$Al$_{0.04}$Si$_{2.03}$O$_5$(OH)$_4$, and Ni ranging from 0.56 to 4.81 wt.% NiO and Fe from 5.26 to 28.58 wt.% Fe$_2$O$_3$. As stated by Golightly & Arancibia (1979), Pelletier (1996) and in Villanova-de-Benavent et al. (2017), serpentine II is enriched in Ni and Fe with respect to serpentine I, however, serpentine II from Yamanigüey contains more Fe than the secondary serpentines reported in these works. Besides, serpentine II is less stoichiometric than serpentine I, which has been linked to vacancies in the octahedral layer, possibly due to the

substitution of Mg by Fe^{3+} (Golightly & Arancibia, 1979; Villanova-de-Benavent et al. 2017). In addition, long and thin magnetite aggregates


Figure 2. Backscattered electron (BSE) images of serpentine II (Srp II) veinlets and pseudomorphs after olivine and pyroxene, crosscut by garnierite (Gar) veins.

frequently occur along some of the serpentine veinlets (remnants of the primary serpentine mesh of the bedrock). There are also rounded subhedral, partially altered, Cr-spinel grains.

The most notable feature in this horizon is the presence of micrometre-thick garnierite veins that crosscut the serpentine matrix (Figure 2). These garnierites yield 39.56-52.53 wt.% SiO_2, 10.92-32.49 wt.% NiO and 0.52-11.0 wt.% Fe_2O_3. They can be classified as mixtures of serpentine and talc-like (a.k.a. *kerolite-pimelite*) garnierites (Figure 3). As observed in Falcondo, the talc-dominated garnierites contain the highest Ni (Figure 3, Villanova-de-Benavent et al. 2016). These veinlets display an oscillatory compositional zoning, with higher Ni contents towards the edges of the vein, and higher Mg contents towards the centre of the vein (Figure 4). This suggests that the precipitation of garnierites is multi-episodic (as in Falcondo, see Villanova-de-Benavent et al. 2014) and that the composition of the percolating aqueous solutions may vary in short periods of time.

The Mn-Ni-Co oxy-hydroxides of the saprolite horizon occur as fibrous crystals overgrowing garnierite (Domínguez-Carretero et al. 2023).

The oxide zone is mostly composed of goethite with minor hematite, gibbsite, Cr-spinel, maghemite, and Mn-Co-Ni oxyhydroxides. Dominant goethite

forms fine-grained aggregates with very little to no cohesion and remarkable porosity. It may occur as botryoidal aggregates or as pseudomorphs of the primary bedrock minerals (e.g., olivine). The mineral chemistry of goethite reveals NiO contents up to 0.81 wt.%. Subhedral Cr-spinel relicts, and small
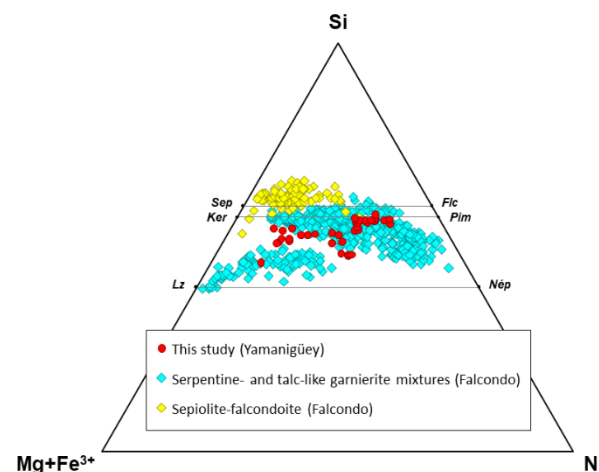
maghemite and hematite grains are found within the goethite matrix. Mn-Ni-Co oxyhydroxides in the oxide zone occur mainly as colloform aggregate grains (Domínguez-Carretero et al. 2023).

Figure 3. Ternary plot representing Mg, Ni and Si in garnierites from Yamanigüey obtained by EMPA (cation proportions calculated on the basis of 100 oxygens). Data from the Falcondo mining district (Villanova-de-Benavent et al. 2014) is shown for comparison.
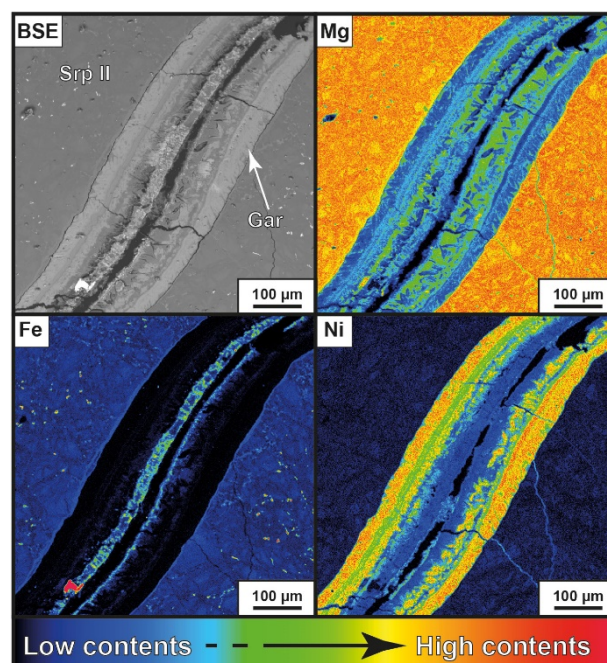
Figure 4. Garnierite (Gar) vein crosscutting serpentine II (Srp II) in a sample from the saprolite horizon of the Yamanigüey deposit, Moa Bay (clock-wise from the upper left): BSE image; and Mg, Ni and Fe X-ray element maps, obtained with EMPA.

5. Final remarks

The studied Ni-laterite profile from Yamanigüey is similar to the hydrous Mg silicate type profiles that have been described in the Falcondo mining district (Dominican Republic, e.g. Villanova-de-Benavent et al. 2017; Tauler et al. 2017) and the ones in New Caledonia (e.g. Wells et al. 2009), in terms of thickness of the saprolite horizon, element distribution along the profile, mineralogy and chemical composition of Ni ores. In fact, it is more similar to those than to the majority of Ni-laterite deposits at Moa Bay, only a few kilometres away. For this reason, more data on the Yamanigüey deposit is necessary in order to shed light on the factors leading to the formation of Ni-Fe-oxyhydroxide- versus Ni-silicate-dominated profiles in the Moa Bay mining district.

Acknowledgements

References

Brand NW, Butt CRM, Elias M (1998) Nickel laterites: classification and features. AGSO J Australian Geol Geoph 17:81–88.

CSA Global Report Nº R117 (2019). Technical Report "Moa Nickel Project, Cuba", NI 43-101. Available at: www.csaglobal.com (Accessed 11.03.2023).

Domínguez-Carretero, D.; Villanova-de-Benavent, C.; Domènech, C.; Proenza, J.A. (2023). Mn-Ni-Co oxy-hydroxides from Ni-Co laterites of Moa-Bay mining district, eastern Cuba. This volume.

Elias, M. (2002). Nickel laterite deposits – geological overview, resources and exploitation. Centre for Ore Deposit Research, University of Tasmania, Special Publication, 4, 205-220.

Golightly, J.P., Arancibia, O.N. (1979). The chemical composition and infrared spectrum of nickel- and iron-substituted serpentine form a nickeliferous laterite profile, Soroako, Indonesia. Canadian Mineralogist 17, 719–728.

Iturralde-Vinent, M.A., García-Casco, A., Rojas-Agramonte, Y., Proenza, J.A., Murphy, J.B., Stern, R.J. (2016). The geology of Cuba: A brief overview and synthesis. GSA Today 26, 4-10.

Lavaut, W. (1998). Tendencias geológicas del intemperismo de las rocas ultramáficas en Cuba oriental. Revista Minera de Geología 15, 9-16.

Lewis, J.F., Draper, G., Proenza, J.A., Espaillat, J., Jimenez. J. (2006). Ophiolite- Related Ultramafic Rocks (Serpentinites) in the Caribbean Region: A Review of their occurrence, Composition, Origin, Emplacement and Nickel Laterite Soils. Geologica Acta 4, 237-263.

Marchesi, C., Garrido, C.J., Godard, M., Proenza, J.A., Gervilla, F., Blanco-Moreno, J. (2006). Petrogenesis of highly depleted peridotites and gabbroic rocks from the Mayarí-Baracoa Ophiolitic Belt (eastern Cuba). Contributions to Mineralogy and Petrology 151(6),717.

Marchesi, C., Garrido, C.J., Bosch, D., Proenza, J.A., Gervilla, F., Monié, P., Rodriguez-Vega, A. (2007). Geochemistry of Cretaceous magmatism in eastern Cuba: recycling of North American continental sediments and implications for subduction polarity in the Greater Antilles Paleo-arc. Journal of Petrology 48, 1813–1840.

Marrero-Leyva, N. (2006). Caracterización Mineralógica del Perfil Saprolítico del Depósito de Lateritas Niquelíferas Yamanigüey. Diploma de Estudios Avanzados, Universidad de Barcelona, 56 pp.

Pelletier, B (1996). Serpentines in nickel silicate ore from New Caledonia. Australasian Institute of Mining and Metallurgy Publication Series – Nickel Conference, Kalgoorlie (Western Australia) 6/96:197–205.

Proenza, J.A., Díaz-Martínez, R., Iriondo, A., Marchesi, C., Melgarejo, J.C., Gervilla, F., Garrido, C.J., Rodríguez-Vega, A., Lozano-Santacruz, R., Blanco-Moreno, J.A. (2006). Primitive island-arc Cretaceous volcanic rocks in eastern Cuba: the Téneme Formation. Geologica Acta 4, 103-121.

Proenza, J.A., Gervilla, F., Melgarejo, J.C., Bodinier, J.L. (1999). Al- and Cr-rich chromitites from the Mayarí-Baracoa ophiolitic belt (eastern Cuba); consequence of interaction between volatile rich melts and peridotites in suprasubduction mantle. Economic Geology 94, 547-566.

Proenza, J.A., González-Jiménez, J.M., Garcia-Casco, A., Belousova, E., Griffin, W.L., Talavera, C., Rojas-Agramonte, Y., Aiglsperger, T., Navarro-Ciurana, D., Pujol-Solà, N., Gervilla, F., O'Reilly, S.Y., Jacob, D.E. (2018). Cold plumes trigger contamination of oceanic mantle wedges with continental crust-derived sediments: Evidence from chromitite zircon grains of eastern Cuban ophiolites. Geoscience Frontiers 9(6), 1921–1936.

Rojas-Agramonte, Y., Garcia-Casco, A., Kemp, A., Kröner, A., Proenza, J.A., Lázaro, C., Liu, D. (2016). Recycling and transport of continental material through the mantle wedge above subduction zones: A Caribbean example. Earth and Planetary Science Letters 436, 93–107.

Tauler, E., Lewis, J.F., Villanova-de-Benavent, C., Aiglsperger, T., Proenza, J.A., Domènech, C., Gallardo, T., Longo, F., Galí, S. (2017). Discovery of Ni-smectite rich saprolite at Loma Ortega, Falcondo mining district (Dominican Republic): geochemistry and mineralogy of an unusual case of 'hybrid hydrous Mg silicate-clay silicate' type Ni-laterite. Mineralium Deposita 52, 1011-1030.

USGS (2021). Mineral Commodity Summaries 2021: US Geological Survey; US Geological Survey: Reston, VA, USA; 200p.

Villanova-de-Benavent, C., Proenza, J.A., Galí, S., García-Casco, A., Tauler, E., Lewis, J.F., Longo, F. (2014). Garnierites and garnierites: textures, mineralogy and geochemistry of garnierites in the Falcondo Ni-laterite deposit, Dominican Republic. Ore Geology Reviews 58, 91–109.

Villanova-de-Benavent, C., Nieto, F., Viti, C., Proenza, J.A., Galí, S., Roqué-Rosell, J. (2016). Ni-phyllosilicates (garnierites) from the Falcondo Ni-laterite deposit (Dominican Republic): Mineralogy, nanotextures, and formation mechanisms by HRTEM and AEM. American Mineralogist 101, 1460-1473.

Villanova-de-Benavent, C., Domènech, C., Tauler, E., Galí, S., Tassara, S., Proenza, J.A. (2017). Fe–Ni-bearing serpentines from the saprolite horizon of Caribbean Ni-laterite deposits: new insights from thermodynamic calculations. Mineralium Deposita 52, 979–992.

Wells, M.A., Ramanaidou, E.R., Verrall, M., and Tessarolo, C. (2009). Mineralogy and crystal chemistry of "garnierites" in the Goro lateritic nickel deposit, New Caledonia. European Journal of Mineralogy, 21, 467–483.